Sandy beaches' chaos: shoreline-sandbar coupling inferred from observational time series

Marius Aparicio[*1], Sylvain Mangiarotti[3], Salomé Frugier[2], Laurent Lacaze[1], Marcan Graffin[2], and Rafael Almar[2]

[1]IMFT, Toulouse, France
[1]Institut de Mécanique des Fluides de Toulouse (IMFT), Université de Toulouse, CNRS, Toulouse, France
[2]LEGOS (CNRS-IRD-CNES-University of Toulouse), Toulouse, France
[3]Université de Toulouse/UT-CNES-CNRS-IRD-INRAE, Centre d'Études Spatiales de la Biosphère, 18 avenue Édouard Belin, 31401 Toulouse, France

Abstract. Sandy shoreline–sandbar systems exhibit complex variability arising from the interplay between hydrodynamic forcing and intrinsic morphological feedbacks. Using long-term satellite-derived shoreline and sandbar observations, we applied global polynomial modeling to reconstruct low-dimensional deterministic dynamics for four contrasting coastal sites. The resulting autonomous models reproduce key morphodynamic features, including self-sustained shoreline oscillations, shoreline–sandbar coupling, and intermittent transitions between quasi-stable configurations. Nonlinear stability analyses reveal that these systems behave as chaotic oscillators, characterized by locally divergent yet globally bounded trajectories. Energetic episodes correspond to rapid shoreline–sandbar exchanges, whereas long low-energy states reflect stable attractor confinement. Together, these results demonstrate that sandy coasts are governed by deterministic but chaotic dynamics, in which internal coupling and self-organization control both variability and finite predictability. The proposed framework offers a physically consistent and data-driven approach to characterize and compare coastal morphodynamics within a unified nonlinear dynamical perspective.

1   Introduction

Systems in geosciences are inherently complex, nonlinear, and often display sensitivity to initial and boundary conditions, leading to behaviors that range from quasi-periodic or near-periodic oscillations to low-dimensional chaos and high-dimensional stochastic-like dynamics (Lorenz, 1963; Dijkstra, 2013; Jin et al., 1994; Nicolis and Nicolis, 1991). Such systems are typically governed by the interplay between internal feedbacks and external forcing (Ghil and Sciamarella, 2023; Maraldi et al., 2025; Di Capua et al., 2023), operating across multiple spatiotemporal scales (Lovejoy, 2019). The ocean–atmosphere system, river deltas, dune fields, and coastal morphodynamics all exemplify this type of nonlinear organization, where irregularity coexists with underlying low-dimensional dynamics (Baas, 2002; Coco and Murray, 2007; Murray et al., 2009, 2014; Jerolmack and Paola, 2010). In particular, coastal environments represent a natural laboratory for studying nonlinear self-organization

[*]Corresponding author: marius.aparicio@imft.fr

under continuous external forcing, as they integrate hydrodynamic energy input (waves, tides, sea level anomalies), sediment transport, and morphological feedback loops within a dynamically evolving boundary system (Castelle and Masselink, 2023).

Recent advances in satellite Earth observation now make it possible to monitor coastal morphology at unprecedented spatiotemporal scales (Vos et al., 2020, 2023; Almar et al., 2023; Graffin et al., 2025a; Frugier et al., 2026; Luijendijk et al., 2018; Castelle et al., 2023; Konstantinou et al., 2023). Time series of shoreline and active nearshore sandbar positions can be extracted from optical satellite imagery, enabling continuous monitoring of beach morphology over decadal timescales with weekly to monthly resolution. These remote sensing observations have now been extensively validated against in-situ field surveys at several historical sites for shoreline data (Graffin et al., 2025b; Vos et al., 2023) and at one site for sandbar data (Frugier et al., 2026, 2025), demonstrating their capacity to resolve the coevolution of the shoreline-sandbar system. The resulting datasets provide, for the first time, sufficiently long and coherent records to analyze the internal dynamics of beach systems.

In parallel, data-driven modeling approaches have emerged as a powerful complement to process-based models for exploring the intrinsic dynamics of complex geophysical systems (Guo et al., 2025; Brunton et al., 2016; Simmons and Splinter, 2025). Among these and derived from the theory of non-linear dynamical systems, the global modeling technique aims to reconstruct deterministic dynamical systems directly from observational time series, without making strong assumptions about predefined governing equations, and has shown promising results from both synthetic (Gouesbet and Letellier, 1994; Aguirre and Letellier, 2009; Mangiarotti and Huc, 2019; Letellier et al., 2009), experimental (Letellier et al., 1995) and real world data (Mangiarotti and Le Jean, 2023; Mangiarotti et al., 2016; Mangiarotti, 2015). One of the few existing frameworks offering a semi-automated implementation of the global modeling approach is the Global Polynomial Modeling (GPoM) package (Mangiarotti et al., 2012). Developed in R, this package integrates a suite of algorithms designed to reconstruct low-dimensional deterministic systems directly from time series. GPoM identifies parsimonious polynomial equations capable of reproducing the observed phase-space geometry and attractor structure by iteratively selecting the minimal subset of nonlinear terms that preserves the variance and structural properties of the reconstructed trajectories. This procedure provides an interpretable representation of the underlying feedbacks and coupling mechanisms between variables involved, and enables testing for deterministic structure within empirical dynamical systems. Such an approach is particularly relevant given that inferring the underlying dynamics of chaotic geophysical systems from noisy and incomplete observations remains a fundamental challenge in the environmental context characterized by low predictability (Ruiz et al., 2022; Jardak and Talagrand, 2018).

In this study, we apply GPoM to a multi-site dataset of satellite-derived shoreline and sandbar time series, representing diverse morphodynamic contexts along wave-dominated coasts. We show that, despite differences in local forcing and sedimentary setting, these systems exhibit a common dynamical structure characterized by nonlinear coupling between the shoreline and the sandbar. The recovered equations capture the essential features of the observed oscillations and reveal a regime of chaos, in which the system remains bounded but sensitive to perturbations. Furthermore, by comparing the reconstructed feedback loops across sites, we propose a preliminary typology of shoreline-sandbar systems, depending on their coupling direction and mechanisms. These results suggest that low-dimensional nonlinear models can provide an interpretable framework for understanding and classifying beach internal dynamics.

55 The remainder of the paper is structured as follows. Section 2 describes the dataset and the methodology for GPoM usage. Section 3 presents the model validation and physical interpretation. Section 4 summarizes the main conclusions and outlines future research perspectives.

2 Methods

2.1 Dataset

2.1.1 Satellite images

The Python API of Google Earth Engine (GEE) was used to download satellite images, providing access to publicly available Top Of Atmosphere (TOA) reflectance images (Level-1C) from various collections (Gorelick et al., 2017; Chander et al., 2009). Sentinel-2 images with a 10-m resolution and 5-day revisit time were downloaded for the four sites: Torrey Pines, Ensenada, Duck and Gold Coast. The blue (B), green (G), and red (R) bands corresponding to visible light wavelengths, the Near-InfraRed (NIR) band just beyond visible red, and the Short-Wave InfraRed (SWIR1 and SWIR2) bands covering longer wavelengths beyond NIR, were downloaded. Bicubic interpolation was applied to the SWIR1 and SWIR2 bands, which originally have a 20 m resolution and are resampled to 10 m resolution like the other bands. To further refine the data quality, a cloud cover threshold was applied using GEE's built-in tools. However, this threshold applies to the entire satellite image tile, which may result in rejecting images that are cloud-free in the Region Of Interest (ROI). To address this issue, all images with total cloud cover below 90% were included in our analysis, and a custom function developed by Graffin et al. (2025a) was applied to filter out images with cloud cover specifically within the ROI.

2.1.2 Satellite-derived shoreline position

The shoreline is detected and extracted using the method developed by Bergsma et al. (2024), specifically designed for sandy beaches. This approach combines a multi-spectral index, the Subtractive Coastal Water Index (SCoWI) with Otsu's threshold refinement method and Marching Squares algorithm to derive sub-pixel shoreline positions (Otsu, 1979; Cipolletti et al., 2012) as:

$$\text{SCoWI} = \text{B} + 2 \times (\text{G} - \text{NIR}) - 0.75 \times \text{SWIR1} - 0.5 \times \text{SWIR2}, \tag{1}$$

where B, G, NIR, SWIR1 and SWIR2 represent the reflectance values of the respective spectral bands: blue, green, near-infrared, short-wave infrared 1 and 2. The shoreline proxy corresponds to the waterline, which reflects variations in sea level including minor tidal effects, as well as other sea-level fluctuations occurring across different timescales.

2.1.3 Satellite-derived sandbar position

Unlike the shoreline, sandbars are submerged features and cannot be directly observed. However, their presence induces wave breaking when incident waves are energetic enough to shoal and dissipate over the bar. The resulting foam pattern provides a visual signature that can be used to infer the sandbar position. Lippmann and Holman (1989) were the first to exploit video imagery to track sandbar positions through time-averaged sequences (time-exposures). Similarly, following the principle of the SCoWI index developed for shoreline detection, the SandBar Index (SBI) proposed by Frugier et al. (2025) automatically identifies and extracts sandbar positions by maximizing the contribution of high-intensity (breaking) pixels while minimizing contributions from other environments (land, sand, and water). However, because the different satellite missions used in this study (e.g., Landsat, VENμS, Sentinel-2) cover distinct radiometric ranges and sensor-specific reflectance characteristics, we introduced a normalized version of the index (NSBI) to ensure methodological consistency and cross-sensor comparability throughout the monitoring period and across all study sites. This normalization allows the reliable detection of breaker zones in satellite imagery and the estimation of sandbar positions through wave-breaking patterns:

$$\text{SBI} = 2 \times (\text{B} - \text{R}) + \text{G} - 0.25 \times \text{NIR}, \tag{2}$$

and:

$$\text{NSBI} = \frac{\text{SBI} - \text{SBI}_{min}}{\text{SBI}_{90} - \text{SBI}_{min}}. \tag{3}$$

Normalization is applied using the 90th percentile (SBI_{90}) of the data rather than the absolute maximum to remove outliers influence, such as excessive reflections or sensor errors, which do not represent typical conditions. A threshold of NSBI > 1.2 allows the identification of breaking zones within a given region of interest and has been shown to be valid across different sites and satellite missions (Frugier et al., 2025, 2026).

2.1.4 Transects

Transects were manually constructed within *QGIS* framework (QGIS Development Team, 2025) by first drawing a baseline along the landward edge of the beach, following its shape, and then generating perpendicular transects directed seaward with origin on land and spaced 30 m apart with lengths adapted to each beach.

2.1.5 SDS and SDSb time series

Waterlines were projected onto the cross-shore transects and the shoreline position x_s was measured along each transect relative to its land origin. The mean shoreline position $\overline{x_s}$ across all transects was then estimated for each satellite image, producing the Satellite-Derived Shoreline (SDS) time series. Breaking lines were projected onto the same transects, and the breaking position x_b was measured relative to the land origin. As wave breaking is instantaneous, its spatial pattern can differ between transects.

On single-bar beaches, some transects show breaking over the bar while others do not; on double-bar beaches, breaking may occur at the inner bar and/or at the outer bar (Wright and Short, 1984). To consistently identify the offshore breaking associated with the bars, K-means clustering was applied along the cross-shore axis. Only well-separated clusters (silhouette score > 0.65) were retained. Within each reliable cluster, breaking positions were extracted, and the offshore cluster was selected. When clustering was unreliable, a single breaking line was assumed. The mean sandbar position $\overline{x_b}$ across all transects was then computed for each satellite image, capturing the representative active sandbar position. Clusters were considered valid only if at least 20% of transects exhibited breaking; otherwise, they were discarded and the next well-separated offshore cluster was evaluated in the same way. The resulting Satellite-Derived Sandbar (SDSb) time series therefore reflects the typical offshore breaking position associated with sandbars. The time series start just before 2018 as between 2015 and 2018, only Sentinel-2A was operating, providing very sparse data.
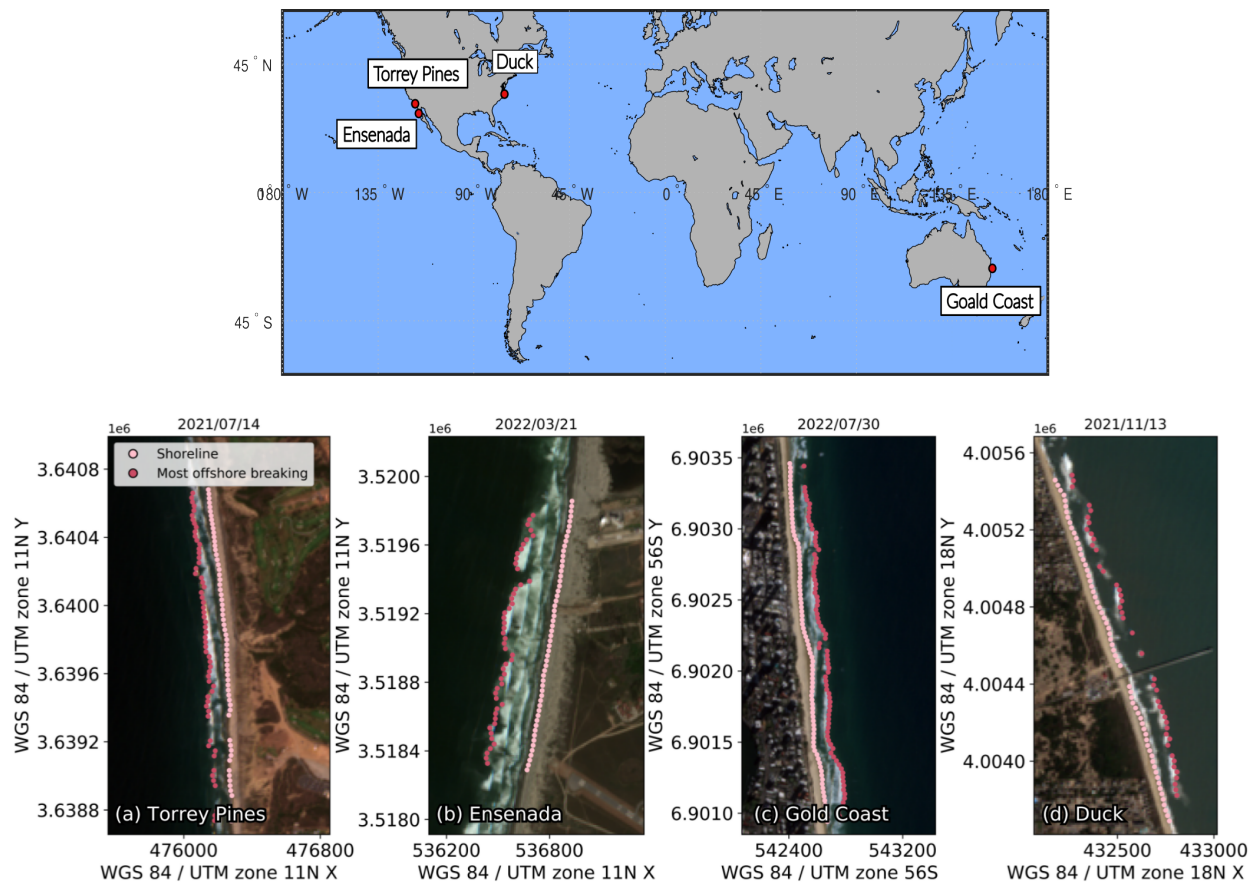
Figure 1. Study sites locations along with illustrative snapshot of the shoreline and sandbar detection via satellite imagery. Each beach is presented on a specific date: **(a)** Torrey Pines (2021/07/14), **(b)** Ensenada (2022/03/21), **(c)** Gold Coast (2022/07/30), and **(d)** Duck (2021/11/13). Imagery © 2022 CNES/Airbus, Map data © 2022 Google.

Fig. 1 shows the geolocation of the four sites along with Sentinel-2 images highlighting the detection of the shoreline (x_s,
light pink) as well as the submerged active sandbar (x_b, offshore breaking, dark pink) along the transects for each beach on a
specific date.

2.2 Sites overview

The four study sites capture a range of morphodynamic conditions along wave-dominated sandy coasts: Torrey Pines (Califor-
nia, USA) is a medium-grained barred beach ($D_{50} \approx 0.2$ mm) backed by steep cliffs and influenced by complex wave refraction
from offshore islands (Ludka et al., 2019). Yearly-averaged significant wave height conditions are $H_s \approx 1$–1.5 m with peak
periods of $T_p \approx 10$–12 s. Ensenada Beach (Baja California, Mexico) is an intermediate mesotidal system with a single active
sandbar ($D_{50} = 0.25$ mm) responding to a bimodal swell regime: energetic north-westerly winter waves (H_s up to 4 m) and
milder south-westerly summer waves ($H_s \approx 0.7$ m) (Ruiz De Alegría-Arzaburu and Vidal-Ruiz, 2018). Duck (North Carolina,
USA) is a double-bar beach exposed to high-energy Atlantic forcing ($H_s \approx 1.2$–1.8 m, $T_p \approx 8$–10 s) exhibiting strong seasonal
variability in sandbar dynamics (Lippmann and Holman, 1990). Gold Coast (Queensland, Australia) is a double-barred quartz-
sand beach ($D_{50} \approx 0.25$ mm) exposed to persistent south-easterly swells ($H_s \approx 0.8$ m, $T_p \approx 9$–10 s) and an intense northward
littoral drift of about 5×10^5 m³/yr (Price et al., 2011).

Together these sites encompass the principal morphodynamic regimes described by Wright and Short (1984) and Masselink
and Short (1993): from micro- to mesotidal, single- to double-bar, and reflective to dissipative states, forming a coherent natural
laboratory for analyzing shoreline–sandbar coupling.

2.3 Data preprocessing

To account for local 3D-variability, we computed the mean shoreline and sandbar positions ($\overline{x_s}, \overline{x_b}$) across all available transect
using a robust interquartile range (IQR) estimator (Whaley III, 2005), which mitigates the influence of outliers and ensures
stability in the composite signal, particularly during energetic events or data gaps. Because satellite-derived shoreline and
nearshore sandbar positions exhibit different levels of noise, typically higher for the sandbar as the variability of offshore
breaking is much more sensitive to stochastic day-to-day variations in wave forcing, temporal smoothing windows were indi-
vidually adjusted to retain intra-seasonal to interannual variability (typically 1–3 months smoothing) while filtering out high-
frequency noise. The resulting time series were then standardized (zero mean, unit variance) and resampled onto a common
daily grid using spline interpolation to ensure continuous and smooth first- and second-order temporal derivatives, yielding a
single representative time series for shoreline and sandbar positions at each site (Fig. 2).
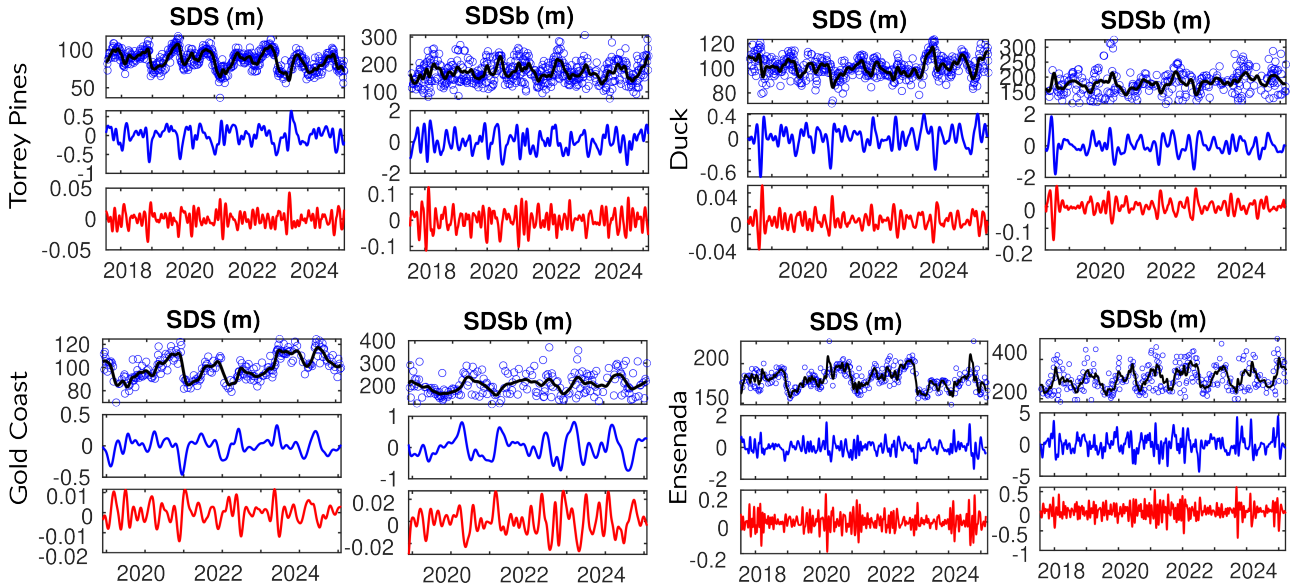
Figure 2. Study sites time-series overview. Satellite-derived shoreline (SDS) and nearshore sandbar (SDSb) time series and their first- and second-order temporal derivatives (blue and red, respectively) for the four study sites: Torrey Pines (USA), Gold Coast (Australia), Ensenada (Mexico) and Duck (USA). Raw daily observations (blue dots) and smoothed trajectories (black lines) are shown together with the corresponding time derivatives computed using a Savitzky–Golay filter.

2.4 Global modeling using GPoM

The global modeling approach provides a fully data-driven framework to retrieve a minimal set of ordinary differential equations (ODEs) capable of reproducing, from observations, both the temporal trajectories (over short timescales) and the set of states toward which the system evolves over time, without prior assumptions about the underlying physical processes (Mangiarotti and Huc, 2019).

2.4.1 Concept and theoretical background

According to the embedding theorem of Takens (1981), the dynamics of a deterministic system can be reconstructed from a limited number of observables by using either delays, time derivatives, or a combination of both (Sauer et al., 1991), provided that the embedding dimension is sufficiently large and the observability of the variables (i.e. the amount of information about the system dynamics contained in each observable) is sufficiently high (Aguirre et al., 2018; Letellier et al., 2018). Global modeling exploits this principle to infer the functional form of the governing equations as:

$$\frac{dX_i}{dt} = \sum_{j=1}^{N_p} K_{ij} \Phi_j(X_1, X_2, \ldots, X_m), \qquad i = 1, \ldots, m, \tag{4}$$

where X_i denotes the i-th state variable (with m the total number of variables), $\Phi_j(X_1, X_2, \ldots, X_m)$ denotes the j-th polynomial monomial constructed from the state variables up to degree $d_{\max}$ (e.g., X_1^2, $X_1 X_2$, X_2^3, etc.), forming the functional basis

160   of the model, and K_{ij} the coefficients estimated by linear regression. Each equation thus represents the temporal evolution of one variable as a polynomial combination of all others.

In practice, time derivatives of the observables are estimated through Savitzky–Golay filtering, which preserves local polynomial consistency and minimizes noise amplification in comparison to finite-difference schemes (Ahnert and Abel, 2007). The resulting derivatives (Fig. 2) form the basis for constructing candidate differential equations, which are then combined into
165   a full dynamical system.

2.4.2 Implementation in the GPoM package

The GPoM package (Mangiarotti et al., 2012; Mangiarotti and Huc, 2019) implements this approach in R and provides a semi-automated framework for model discovery, selection, and validation. It systematically explores combinations of polynomial terms given the number of state variables m, the maximum polynomial degree $d_{\max}$, and the maximum derivative order.
170   Each candidate model is numerically integrated and compared with observations using statistical and geometric criteria such as variance preservation, correlation between observed and simulated variables, as well as structure reliability of the reconstructed attractor in the phase space.

By iteratively selecting the most informative, dynamically consistent, and parsimonious subset of terms, GPoM builds low-dimensional polynomial models that capture the essential nonlinear coupling and feedback mechanisms among variables (Mangiarotti et al., 2025).
175   These models can then be used to investigate the deterministic structure of the system, assess its stability properties, and explore potential bifurcations or chaotic regimes emerging from the coupled dynamics.

In this study, GPoM is applied to the coupled evolution of shoreline and active sandbar systems. The objective is to identify minimal polynomial models capable of reproducing the observed phase-space geometry and the dynamical interplay between shoreline position and sandbar migration, thereby revealing the feedbacks governing coastal morphological variability.

180   ### 2.5 Protocol

In order to explore system complexity and potential chaos, model dimensions $m = 3$ and $m = 4$ were tested within GPoM, with polynomial degree ranging from $d_{\max} = 2$ to 4. According to the Poincaré–Bendixson theorem, continuous autonomous systems of dimension $m \leq 2$ can only display a very low level of complexity, as their trajectories are confined to fixed points or period-1 limit cycles (Poincaré, 1893), thus precluding the stretching and folding dynamics required for chaos (Gilmore and
185   Lefranc, 2002). Hence, higher-dimensional embeddings ($m \geq 3$) were explored to enable the capture of complex feedbacks and non-trivial oscillatory regimes. All possible variable combinations among (X_1, X_2, X_3, X_4) satisfying $m = 3$ or 4 were systematically explored after truncating 100 days from both ends of the time series to minimize edge effects associated with smoothing and derivative estimation. Each final model was thus inferred from approximately 95% of the total record length (~ 10 years of Sentinel-2 revisits), which, in cases where robust deterministic models were obtained, provides strong evidence
190   for determinism within the real-world data dynamics. A moving window of $\omega = 51$ days was used for derivative smoothing using the Savitzky–Golay filter. Sensitivity tests around this window size showed no significant change in the resulting model structure, confirming the robustness of the reconstruction. The number of polynomial terms K (Eq. (4)) allowed in the models

was set between $K = 6$ and $K = 26$, covering a broad range of configurations while limiting overfitting due to excessively complex models. Finally, candidate models that were neither fixed points nor simple limit cycles and remained numerically stable for at least 80 years of integration were visually inspected. Model quality was primarily assessed through phase-space consistency and amplitude preservation rather than pointwise prediction accuracy, as GPoM aims to reproduce the system's underlying geometry rather than forecast individual states. Among these, the most parsimonious model (i.e., the one with the smallest combination of K, m, and $d_{\max}$) was retained for further dynamical analysis.

Repeated runs with slightly perturbed preprocessing parameters yielded consistent model structures, suggesting that the inferred couplings are robust features of the underlying dynamics.

3 Results

3.1 Model–data comparison and spectral validation

3.1.1 Phase space projections

The phase spaces derived from the GPoM autonomous models (see system equations in SubSec 3.2) closely reproduce, both in term of amplitude and density occupation, the observed dynamics of shoreline–sandbar systems across all study sites (Fig. 3). For the three-dimensional models (Gold Coast, Torrey Pines, Ensenada), each projection of the attractor reveals a coherent morphodynamic coupling between shoreline position (X_1), its temporal derivative (X_2), and sandbar position (X_3). At Torrey Pines and Ensenada (Eqs. (5), (7)), the system oscillates along a quasi-linear negative correlation between shoreline and sandbar positions (X_1–X_3) at seasonal timescales, consistent with a coupled retreat–recovery mechanism: when wave energy increases during winter, the sandbar migrates offshore while the shoreline retreats. This correlation suggests that the sandbar response is not fast enough to dissipate the enhanced wave energy, reducing its protective role and leading to greater shoreline retreat. During calmer periods, the sandbar slowly migrates landward, promoting shoreline recovery and closing the oscillatory cycle captured by the model. In contrast, the Gold Coast system (Eq. (6)) displays an inverted correlation pattern, showing that the shoreline-sandbar system evolves as one, responding similarly to incoming forcing.

For the three models, the (X_2–X_1) portrait is the typical projection of a differential phase space involving an observable and its first-order derivative (Fig. 3). In such a representation, the shape of the trajectory reflects the underlying restoring and dissipative mechanisms of the system. The attractors observed here indicate a combination of two oscillatory processes in which shoreline position (X_1) oscillates around a single equilibrium point for Torrey Pines and Ensenada, under the restoring action of sandbar-mediated feedbacks and the cyclicity imposed by the annual cycle. For Gold Coast, the attractor evolves around two equilibrium points (located close to $(-1, 0)$ and $(1, 0)$ in the (X_1, X_2) projection), and a third one situated between them (close to $(0, 0)$), which enables alternation between the two equilibria or the emergence of larger loops connecting them. The amplitude of the loops provide insight into the system's stability and rate of energy exchange. Extended, large-amplitude loops indicate stronger seasonal variability and larger-scale shoreline adjustments, whereas numerous smaller, short-lived loops reflect disruptive short-term events (e.g., storms, intra-seasonal variability). The amplitude of these smaller loops further reveals

225   the system's capacity to damp the morphological imprint of such disturbances, thus reflecting its resilience. At Torrey Pines, the observational data (dark blue within Fig. 3) exhibit wide, extended loops involving two main branches, indicative of a highly energetic system dominated by strong seasonal variability and pronounced morphological exchanges. The numerous more rounded shorter loops suggest a superimposed contribution of storm-scale fluctuations. The model reproduces the overall extent of the attractor, capturing the main envelope of variability and the large-scale cyclic behavior, but with smoother

230   trajectories, implying that part of the short-term perturbations and their damping–recovery dynamics are smoothed (i.e. high dimensional dynamics associated with noise has been filtered). The dynamical complexity observed at Torrey Pines ultimately converges to a period-two cycle, suggesting a metastable chaotic regime that may be triggered by temporary variations in the system (e.g. tides, mesoscale eddies, coastal storms). In contrast, at both Gold Coast and Ensenada, the model successfully reproduces the occurrence of both small and large loops, suggesting a more representative behavior across the system's

235   spatiotemporal scales. The $(X_3–X_2)$ projection highlights the joint variability between sandbar position and shoreline rate of change, reflecting the co-evolution of both components within the same morphodynamic feedback loop. The sandbar position (X_3) encapsulates the system's longer-term adjustment to hydrodynamic conditions, while the shoreline rate (X_2) expresses the more immediate response of the beach. The attractor geometry thus encompasses the phase relationship between these two timescales (making it the less evident projection to interpret only through observations). At Torrey Pines, Gold Coast

240   and Ensenada, the trajectories form elongated, looping structures, indicating that sandbar migration and shoreline motion are phase-shifted, with delayed recovery of the shoreline once the sandbar returns landward. This reflects a coupled oscillatory system where energy is alternately stored in sandbar migration and released through shoreline adjustment. Therefore, these portraits reveal the mutual, rather than unidirectional, influence between the sandbar and shoreline components of the system for all three sites.

245   The four-dimensional model obtained at Duck exhibits a markedly more intricate phase-space organization, with multiple intertwined trajectories and a complex structure reflecting strong nonlinear coupling among the shoreline, sandbar, and their respective derivatives (X_2, X_4). In the $(X_2–X_1)$ projection, broad nested loops and secondary sub-cycles indicate an oscillator governed by several interacting timescales, consistent with a system where rapid morphological responses are superimposed on slower morphodynamic adjustments. The $(X_3–X_1)$ projection displays a folded, asymmetric attractor in which the trajectory

250   slope reverses across the domain. This departure from the more linear correlation observed at other sites suggests that the coupling between shoreline and sandbar is not stationary but alternates between regimes of weak and strong interaction. In the $(X_3–X_2)$ plane, spiral-like loops around the origin denote delayed responses between sandbar position and shoreline velocity as the shoreline adjusts to sandbar migration with a phase lag. The amplitude variability within these spirals reflects intermittent shifts in coupling strength, possibly associated with episodic energetic events or memory effects in sediment redistribution.

255   The $(X_4–X_1)$ projection, linking shoreline position to sandbar migration rate, reveals a pronounced asymmetry: rapid offshore sandbar motion $(X_4 < 0)$ corresponds to abrupt shoreline retreat, whereas onshore sandbar migration $(X_4 > 0)$ is associated with a slower and more gradual recovery. This hysteresis indicates that the system retains a morphodynamic memory of past energetic states and/or that the threshold required to trigger significant morphological change depends on whether energy is increasing or decreasing. The $(X_4–X_2)$ projection reveals a nonlinear relationship, showing that shoreline and sandbar

velocities are not independent. Their interaction varies with the system state, suggesting a potentially intermittent coupling. The (X_3-X_4) projection isolates the intrinsic sandbar dynamics, showing concentric, nested cycles that are typical of systems organized around two main pseudo-periods. The observed dynamics are not quasi-periodic but may derive from such behavior, suggesting toroidal chaos.

The high complexity of the Duck model derived using GPoM is consistent with field observations of sandbar dynamics, where the inherited fall morphology exerts a strong control on the subsequent year's morphological evolution (Anderson et al., 2023). This behavior reflects a pronounced sensitivity to initial conditions, as the pre-existing sandbar configuration constrains the system's response to comparable hydrodynamic forcing, leading to path-dependent and potentially hysteresis dynamics. Moreover, Duck belongs to a beach type characterized by an active sandbar that slowly migrates offshore with aperiodic consistency, before being replaced by a newly active bar forming at the breaker line ; a behavior commonly referred to as Net Offshore Migration (NOM) (Ruessink et al., 2009). In this study, only the active sandbar is considered, and therefore this phenomenon does not explicitly appear within our dataset. Nevertheless, this additional level of complexity may not be uncorrelated with the complex attractor geometry and higher-order nonlinear terms revealed by the model as the NOM behavior is known to be strongly conditioned by the antecedent beach state (Plant et al., 1999; Ruessink et al., 2003), which could reflect the memory and cumulative effects inherent to these episodic-to-interannual bar exchanges.

Broadly, the modeled attractors successfully reproduce the geometry of the observed systems, capturing their characteristic oscillatory loops, asymmetries, twisting and folding, and state-dependent variability. The models were integrated over extended periods (80 years) to assess their numerical stability and to allow the full attractor to unfold in phase space. As a result, the system may occasionally visit states that were not sampled during the observational time window, yet remain dynamically consistent with the reconstructed equations. This property illustrates the model's ability to generalize beyond the training dataset while preserving its intrinsic dynamical organization.
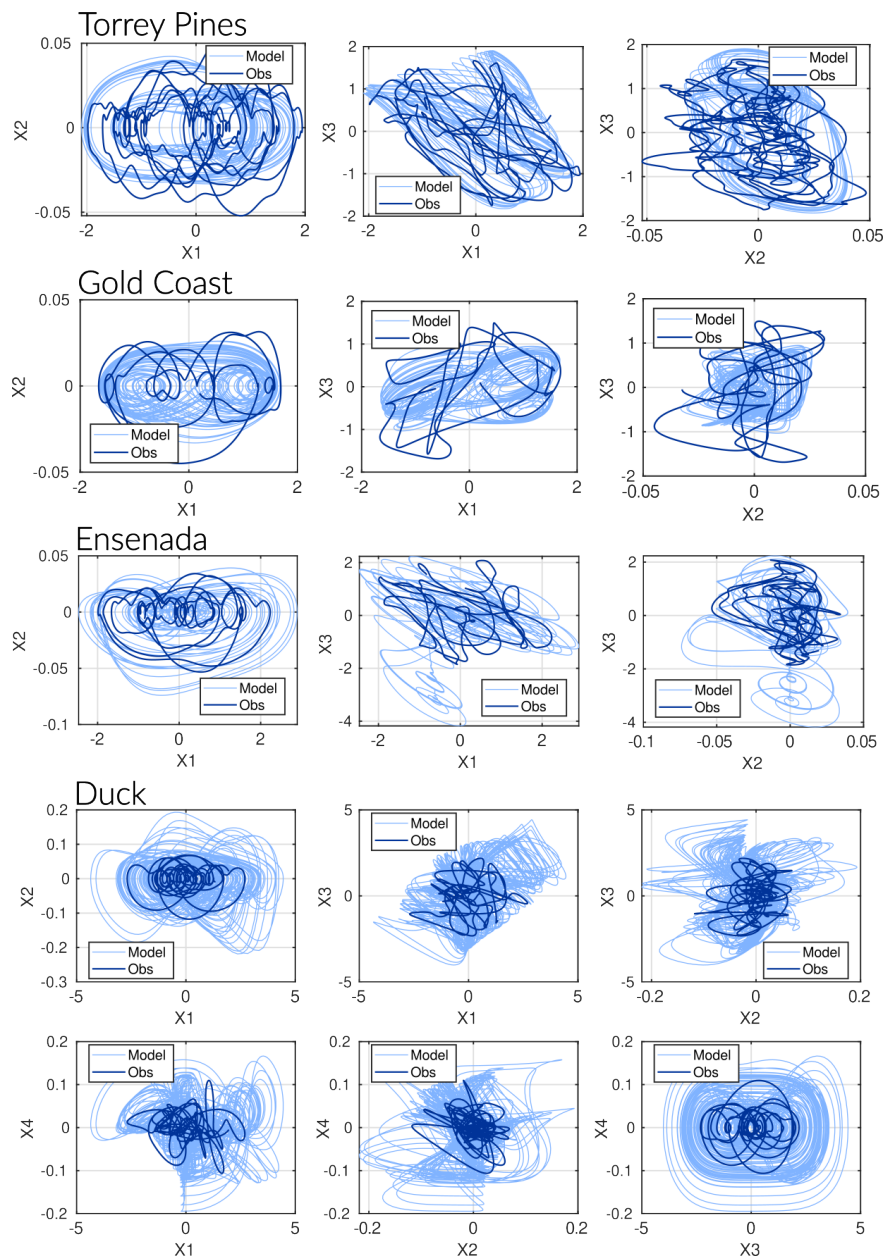
Figure 3. Comparison of observed (dark blue) and modeled (light blue) phase spaces. For the three-dimensional models (Gold Coast, Torrey Pines, Ensenada), each portrait of the reconstructed attractor is shown. All systems exhibit a coherent shoreline–sandbar (X_1–X_3) coupling, with a clear negative linear relationship in Torrey Pines and Ensenada, whereas Gold Coast displays an inverted correlation pattern at seasonal scale. The four-dimensional model (Duck) reveals a markedly more intricate structure, characterized by strong nonlinear interactions among variables and the absence of any simple linear dependency between shoreline and sandbar positions (X_1–X_3). The inferred GPoM models successfully reproduce site-specific attractors and capture the essential geometry of the underlying morphodynamic phase space.

3.1.2 Models spectral validation

The spectral analysis provides a detailed verification of the temporal consistency between observed and modeled dynamics (Fig. 4). For each site, the normalized power spectra of the modeled variables (light purple) closely reproduce those derived from the observations (light orange) over several orders of magnitude in frequency. At low frequencies (10^{-4}–$10^{-3}\,\mathrm{day}^{-1}$), the models capture the slow morphodynamic components associated with long-term shoreline–sandbar co-variability, reflecting the system's memory and adjustment at interannual timescales. At intermediate frequencies (10^{-3}–$10^{-2}\,\mathrm{day}^{-1}$), both observed and modeled spectra exhibit distinct shoulders or inflection points, corresponding to the annual to intra-seasonal response of the system to modulations in wave energy. This indicates that the inferred equations successfully embed the transfer mechanisms linking external forcing to shoreline–sandbar exchanges. At higher frequencies ($> 10^{-2}\,\mathrm{day}^{-1}$), the energetic slope remains consistent between models and observations, without evidence of artificial energy accumulation or damping. The fact that the model spectra maintain realistic decay at small scales demonstrates that the deterministic GPoM formulations can mimic the natural dissipation of energy across scales even in the absence of explicit stochastic forcing.

To quantitatively assess model–data fidelity, the comparison of spectral slopes and correlations provides a complementary validation of the models' dynamical realism (Fig. 5). Across all sites, the spectral exponents derived from the models remain consistent with those obtained from the observations, confirming that both share similar scaling laws and temporal persistence ($\alpha \approx 2.5$–4). Spectral correlations exceeding $r > 0.8$ in most cases indicate that the models reproduce not only the dominant frequencies but also the overall energy distribution across temporal scales. Slightly flatter spectral slopes in the modeled series likely reflect the smoothing effect inherent to deterministic low-dimensional reconstructions, which capture organized dynamics but not high-frequency stochastic variability (Mangiarotti et al., 2012, 2016). Nevertheless, the agreement across frequencies spanning more than three decades supports the conclusion that the GPoM-derived equations capture the multiscale organization and memory-driven nature of real shoreline–sandbar dynamics. It is important to note that these models are entirely autonomous: no external forcing has been prescribed, and the variability observed in their dynamics arises solely from the intrinsic couplings reconstructed from the data. The influence of external drivers such as wave climate or sea level modulations is thus implicitly embedded in the model structure itself.

Taken together, these results show that the GPoM models successfully reconstruct the essential physics of the sites observables directly from observational data. They capture the nonlinear coupling between shoreline and sandbar, the characteristic oscillatory attractors, and the broadband red spectral behavior; typical from natural coastal systems (Pianca et al., 2015; Ruessink et al., 2007). The models thus represent compact, deterministic analogs of the observed systems capable of reproducing their key dynamic and statistical properties without external forcing (implicitly embedded in the model structure itself), thereby validating the GPoM approach as a robust framework for identifying the intrinsic dynamics governing shoreline-sandbar evolutions (i.e. the system's response to the forcing input).
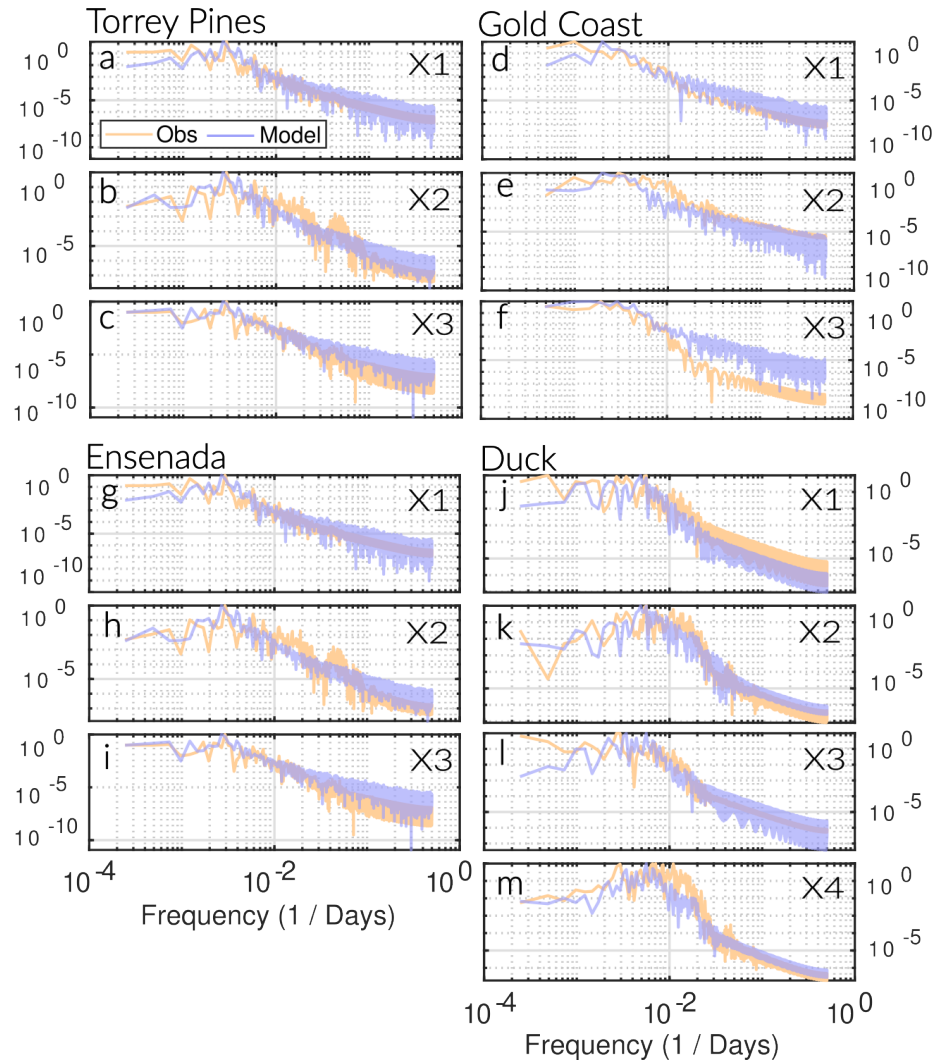
Figure 4. Comparison of normalized spectral power density between observations and models. Each variable's spectrum obtained from the model (light purple) is plotted against its corresponding observation (light orange). The modeled energy distribution closely matches that of the observed data, indicating that the models successfully reproduce the dynamical variability of the systems they were inferred from. At low frequencies (10^{-4}–10^{-3} day^{-1}), the slow components of the shoreline–sandbar system are well captured, reflecting a realistic long-term memory and morphodynamic coupling. The model also reproduces the seasonal to monthly dynamics (around 10^{-2} day^{-1}) with good accuracy. At higher frequencies ($> 10^{-2}$ day^{-1}), the energetic slope remains consistent between model and observations, without overestimation of short-term variability, suggesting that the GPoM-based dynamics naturally filter the high-frequency noise while preserving the dominant physical scales of variability. The broadband power-law spectra ($P(f) \sim f^{-\alpha}$) indicate that the shoreline–sandbar system exhibits long-term memory and self-organized, chaotic dynamics, with energy cascading smoothly from low-frequency morphodynamic cycles to higher-frequency storm-driven responses.
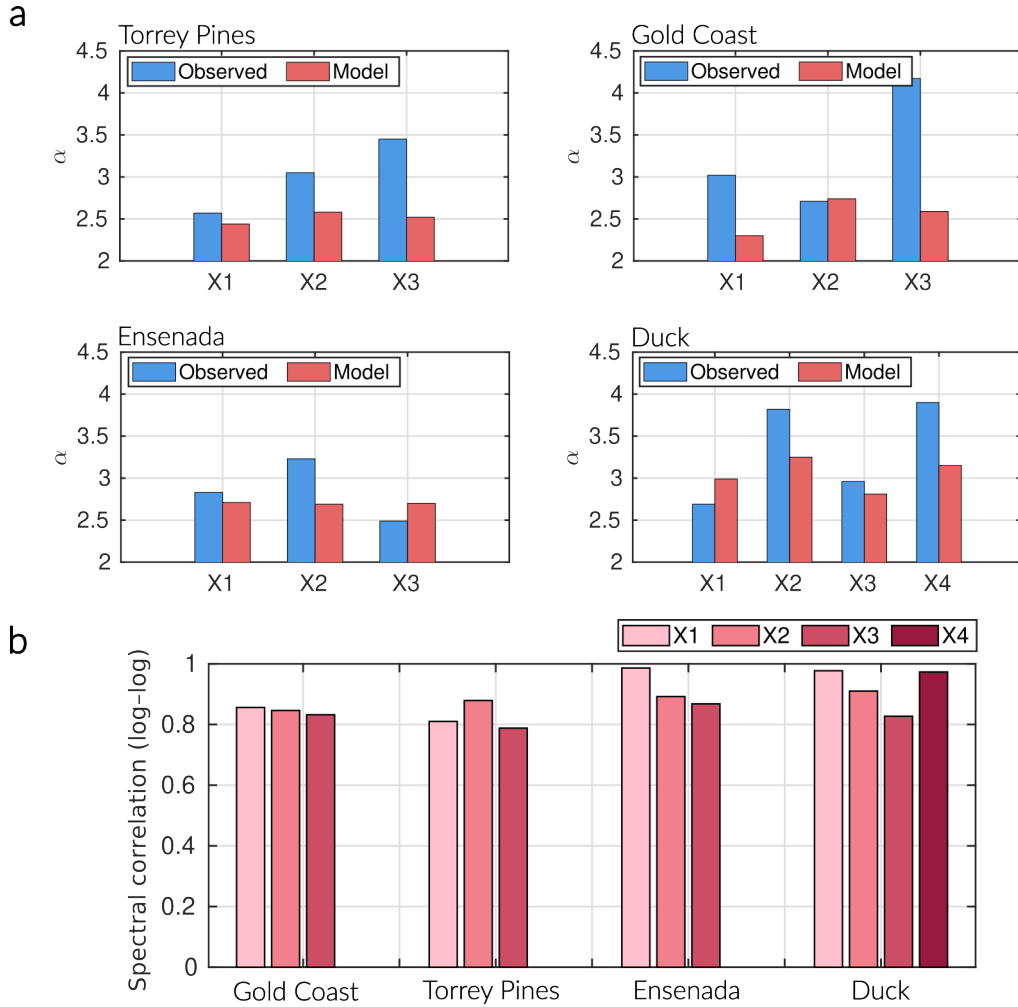
Figure 5. Spectral comparison between observed and modeled dynamics. (a) Comparison of spectral slopes (α) for each variable and site. Both observations (blue) and GPoM models (red) exhibit red-to-brown noise behavior ($\alpha \approx 2.5$–4), indicating scale-invariant, long-memory morphodynamic variability. (b) Spectral correlations (log–log) between observed and modeled spectra show consistently high values ($r > 0.8$), confirming that the inferred nonlinear dynamics reproduce the observed energy distribution across temporal scales. The GPoM models capture both the scaling and spectral energy structure of the shoreline–sandbar systems, reflecting a realistic transfer of energy from low-frequency morphodynamic oscillations to higher-frequency storm-driven variability.

3.2 Reconstructed equations, model structures and physical interpreation of dominant terms

The autonomous polynomial models reconstructed for each site are presented in Eqs. (5)–(8). All systems follow a canonical form in which the first equation expresses the temporal derivative of the shoreline position ($\dot{X}_1 = X_2$), while the subsequent
315 equations describe the nonlinear coupling between shoreline acceleration ($\dot{X}_2$) and sandbar dynamics (X_3, and X_4 for Duck).

Torrey Pines
$$\begin{cases} \dot{X}_1 = X_2, \\[2mm] \dot{X}_2 = a_1 X_3 + a_2 X_3^3 + a_3 X_2 X_3^2 + a_4 X_2^2 X_3 + a_5 X_1 X_3^2 + a_6 X_1^2 X_3 + a_7 X_1^3, \\[2mm] \dot{X}_3 = b_1 + b_2 X_3 + b_3 X_2 + b_4 X_3^3 + b_5 X_2 X_3^2 + b_6 X_2^2 + b_7 X_2^2 X_3 \\[2mm] \qquad + b_8 X_1 + b_9 X_1 X_2 X_3 + b_{10} X_1 X_2^2 + b_{11} X_1^2 X_2. \end{cases}$$ (5)

Gold Coast
$$\begin{cases} \dot{X}_1 = X_2, \\[2mm] \dot{X}_2 = a_1 X_3 + a_2 X_3^3 + a_3 X_2 X_3 + a_4 X_2^2 X_3 + a_5 X_1 + a_6 X_1 X_3^2 + a_7 X_1 X_2^2 + a_8 X_1^2 X_3 + a_9 X_1^3, \\[2mm] \dot{X}_3 = b_1 + b_2 X_3 + b_3 X_2 + b_4 X_2 X_3^2 + b_5 X_1^2. \end{cases}$$ (6)

320   Ensenada:
$$\begin{cases} \dot{X}_1 = X_2, \\[2mm] \dot{X}_2 = a_1 X_3 + a_2 X_1 X_3^2 + a_3 X_2 + a_4 X_1 X_2 + a_5 X_1 X_2 X_3 + a_6 X_1^2 X_3 + a_7 X_1^2 X_2 + a_8 X_1^3, \\[2mm] \dot{X}_3 = b_1 + b_2 X_3 + b_3 X_2 + b_4 X_2^3 + b_5 X_1 X_3^2 + b_6 X_1^2 X_3 + b_7 X_1^3 \end{cases}$$ (7)

Duck:
$$\begin{cases} \dot{X}_1 = X_2, \\[2mm] \dot{X}_2 = a_1 X_4 + a_2 X_3^2 X_4 + a_3 X_2 X_4 + a_4 X_2^2 X_3 + a_5 X_2^3 + a_6 X_1 + a_7 X_1 X_4 + a_8 X_1 X_4^2 \\[2mm] \qquad + a_9 X_1 X_2 + a_{10} X_1 X_2 X_4 + a_{11} X_1 X_2^2 + a_{12} X_1^2 + a_{13} X_1^3, \\[2mm] \dot{X}_3 = X_4, \\[2mm] \dot{X}_4 = c_1 X_3^3 + c_2 X_1 X_2 + c_3 X_1^3. \end{cases}$$ (8)

The reconstructed equations are third-order polynomial systems, containing respectively 19, 15, 16, and 18 K terms for

325   Torrey Pines, Gold Coast, Ensenada, and Duck. Each model combines quadratic and cubic cross-interactions together with self-interacting terms. In these models, feedbacks between shoreline position, sandbar position, and their respective temporal derivatives jointly govern the observed variability. Although several of their respective terms exhibit relatively small amplitudes (Table 1), they contribute critically to the global stability of the reconstructed attractor by shaping its fine-scale curvature and preventing divergence during long integrations. This behavior is consistent with the GPoM algorithm design, which pri-

330   oritizes preservation of the phase-space geometry over direct time-series correlation between data and model (Mangiarotti

et al., 2012). As such, the equations obtained are an approximate and reduced formulation of the original ones. Hence, several physical processes may have been compressed into a single shared monomial, which limits the mechanical interpretation, since each term can no longer be viewed as an independent process. Likewise, complementary contributions may not appear in the equations derived by GPoM, which makes it more difficult to clearly distinguish the physical processes underlying the system dynamics. Consequently, the interpretation should focus on the dominant terms (those with the largest variance within their respective equations) while acknowledging that weaker nonlinearities collectively ensure attractor coherence and long-term stability. Here, for each model, we provide a rewritten form of the equation from a mechanistic viewpoint in terms of the forces $\boldsymbol{F}_i$ applied to the sand masses (Eqs. (9)-(12)), positions $\boldsymbol{X}_i$ and speed $\boldsymbol{V}_i$, and using only the terms with a variance of $Var_{eq} \geq 10\%$ (Tables 2-5), accompanied by fluence diagrams (Fig. 6) to support the physical interpretation. V_1 and V_3 notation are fostered instead of X_2 and X_4 to facilitate the interpretation. The details of these rewritten forms are given in the appendix (see Appendix A).

$$\text{Torrey Pines} \quad \begin{cases} \boldsymbol{F}_1 = -a_7 X_1^2 \boldsymbol{X_1} + a_2 X_3^2 \boldsymbol{X_3} - a_6 X_1^2 \boldsymbol{X_3}, \\ \boldsymbol{F}_3 = -b_3 \boldsymbol{F}_1 - 3b_4 X_3^2 \boldsymbol{V}_3 \end{cases} \tag{9}$$

$$\text{Gold Coast} \quad \begin{cases} \boldsymbol{F}_1 = -a_9 X_1^2 \boldsymbol{X_1} + a_5 \boldsymbol{X_1} - a_1 \boldsymbol{X_3}, \\ \boldsymbol{F}_3 = b_3 \boldsymbol{F}_1 - 2b_5 X_1 \boldsymbol{V}_1 \end{cases} \tag{10}$$

$$\text{Ensenada:} \quad \begin{cases} \boldsymbol{F}_1 = -a_8 X_1^2 \boldsymbol{X_1} - a_6 X_1^2 \boldsymbol{X_3} + a_1 \boldsymbol{X_3}, \\ \boldsymbol{F}_3 = -b_3 \boldsymbol{F}_1 + 3b_4 X_2^2 \boldsymbol{F}_1 \end{cases} \tag{11}$$

$$\text{Duck:} \quad \begin{cases} \boldsymbol{F}_1 = a_4 V_1^2 \boldsymbol{X_3} - a_5 V_1^2 \boldsymbol{V_1} - a_{10} V_1 V_3 \boldsymbol{X_1} - a_{11} V_1^2 \boldsymbol{X_1} - a_8 V_3^2 \boldsymbol{X_1}, \\ \boldsymbol{F}_3 = c_1 X_3^2 \boldsymbol{X_3} + c_3 X_1^2 \boldsymbol{X_1} \end{cases} \tag{12}$$

3.2.1 Torrey Pines

The variance-significant terms contributing to the shoreline dynamics (first equation in Eqs. (9)) highlight both the natural oscillatory behavior of the shoreline and the feedback exerted by the sandbar on its adjustment. The term $-a_7 X_1^2 \boldsymbol{X_1}$ acts as a nonlinear restoring force that drives the shoreline position back toward the imposed equilibrium ($X_1 = 0$). Its cubic dependence

implies a very weak response near equilibrium and a rapidly increasing restoring tendency for large excursions, consistent with the oscillatory behavior typically observed on wave-dominated sandy shorelines in the absence of other major external forcings (Dean, 1991; Yates et al., 2009). In contrast, the term $+a_2 X_3^2 \boldsymbol{X_3}$ introduces a nonlinear destabilizing contribution transmitted from the sandbar dynamics to the shoreline. Because it scales with X_3^3, it strengthens the shoreline response when the sandbar undergoes large displacements. Generally speaking, the sandbar acts as an energy buffer when located close to the shoreline, reducing the effective wave energy forcing reaching the shore, whereas large offshore excursions reduce this buffering capacity and allow stronger forcing to be transmitted to the shoreline. As a result, far-from-equilibrium sandbar positions feed back onto the shoreline as an increasingly strong driving force, pushing its motion away from equilibrium. Finally, the term $-a_6 X_1^2 \boldsymbol{X_3}$ represents a nonlinear cross–coupling between the shoreline position and the sandbar. Because X_1^2 modulates its magnitude, this contribution becomes significant only when the shoreline is strongly displaced. Its sign is controlled by X_3: sandbar excursions generate a forcing on the shoreline that opposes the sign of X_3, thereby acting as a nonlinear corrective influence transmitted from the sandbar to the shoreline.

The equation governing the sandbar dynamics involves two variance-significant terms (second equation in Eqs. (9)). The first one, $-b_2 F_1$, represents an anticorrelated coupling whereby the bar responds in the opposite direction to the forcing applied to the shoreline. Altogether with $-a_6 X_1^2 \boldsymbol{X_3}$, this term captures the seasonal coupling within the shoreline–sandbar system: during winter, offshore sandbar migration accompanies shoreline retreat, while during summer, onshore bar migration accompanies shoreline advance. This behavior reflects an adaptive surf-zone system whose effective dissipation length adjusts to the seasonal modulation of incoming wave forcing, thereby enhancing system resilience between seasonal returns via dynamic feedback. This dynamical interpretation is supported by field observations at Torrey Pines, where the surf-zone width is well preserved between equivalent seasonal states each year (Winant et al., 1975; Aubrey et al., 1980). The second term, $-3b_4 X_3^2 V_3$, acts as a nonlinear damping of the bar motion. Because the dissipation scales with X_3^2, the migration of the sandbar is only weakly damped near its mean position but becomes increasingly inhibited for large excursions. This cubic-like friction prevents unbounded bar migration and reflects the enhanced energy dissipation occurring when the surf-zone width becomes large.

3.2.2 Gold Coast

For the Gold Coast system (Eqs. (10)), the variance-significant terms reveal a shoreline dynamics combining both destabilizing and stabilizing contributions. The cubic term $-a_9 X_1^2 \boldsymbol{X_1}$ acts as a nonlinear restoring force that drives the shoreline back toward its equilibrium, with a weak effect near $X_1 = 0$ and a rapidly increasing restoring action for large excursions. In contrast, the linear term $+a_5 \boldsymbol{X_1}$ introduces a weak intrinsic instability that tends to amplify shoreline displacements. The additional linear coupling term $-a_1 \boldsymbol{X_3}$ reflects a stabilizing sandbar–shoreline feedback: offshore (onshore) bar positions pull the shoreline landward (seaward), acting to counter shoreline excursions rather than reinforce them. This opposite–signed response limits the net shoreline displacement generated by sandbar migration and contributes to the stability of the system.

The sandbar dynamics include two variance-significant terms. The first one, $+b_3 F_1$, represents a direct coupling whereby a fraction of the shoreline forcing is transmitted to the sandbar, depicting a striking difference with Torrey Pines. Here, the surf zone tend to translate rather than extend/shorten, independently of the season, suggesting a surf zone geometry conservation

at Gold Coast. The second one, $-2b_5X_1V_1$, acts as a cross-damping mechanism: the sandbar motion is increasingly inhibited

when the shoreline moves rapidly, indicating a strongly coupled shoreline-sandbar system in which sandbar migration is limited

390   (i.e. lagged in relation to) by the instantaneous shoreline adjustment rather than by its own displacement.

3.2.3   Ensenada

For the Ensenada system (Eqs. (11)), the shoreline dynamics combine a nonlinear intrinsic restoring mechanism with both

stabilizing and destabilizing shoreline-sandbar feedbacks. The cubic term $-a_8X_1^2\boldsymbol{X_1}$ acts as a nonlinear restoring force that

drives the shoreline back toward equilibrium, with weak influence near $X_1 = 0$ and rapidly increasing restoration for large

395   excursions. The nonlinear cross-coupling term $-a_6X_1^2\boldsymbol{X_3}$ reflects a stabilizing influence of the sandbar on the shoreline that

becomes significant only when the shoreline is strongly displaced, indicating a threshold-like buffering role of the sandbar that

depends on its relative position with respect to the shoreline. In contrast, the linear term $+a_1\boldsymbol{X_3}$ introduces a destabilizing

shoreline-sandbar interaction: offshore (onshore) sandbar positions push the shoreline seaward (landward), enhancing rather

than counteracting shoreline excursions.

400   The sandbar dynamics involve two variance-significant terms. The first one, $-b_3F_1$, represents an anticorrelated coupling

whereby the bar responds in the opposite direction to the forcing applied to the shoreline, consistent with a compensatory

sandbar adjustment. The second term, $+3b_4X_2^2F_1$, reflects a velocity-modulated strengthening of the shoreline-to-sandbar

coupling: when the shoreline moves rapidly, the forcing transmitted to the bar is amplified and acts in the same direction as

F_1. As a result, energetic shoreline motion can override the anticorrelated response induced by $-b_3F_1$, causing the sandbar

405   to migrate in the same direction as the shoreline forcing. This mechanism makes the Ensenada sandbar highly responsive to

high-energy disruptive events (e.g., coastal storms): rapid shoreline retreat ($F_1 < 0$, often associated with storm erosion) can

generate an amplified onshore migration of the sandbar ($X_3 < 0$) when shoreline velocities are large, inverting the classical

expectation of offshore sandbar migration during storms.

3.2.4   Duck

410   For Duck (Eqs. (12)), the shoreline dynamics are uniquely controlled by nonlinear velocity–dependent interactions, with no

autonomous restoring or destabilizing term acting directly on the shoreline position. The shoreline dynamics is influenced by

five significant terms which contributes to the complexity of this beach. The term $+a_4V_1^2\boldsymbol{X_3}$ expresses a sandbar–shoreline

feedback that becomes effective only when the shoreline moves rapidly, whereas $-a_5V_1^2\boldsymbol{X_2}$ provides quadratic damping

of shoreline motion. The terms $-a_{11}V_1^2\boldsymbol{X_1}$ and $-a_8V_3^2\boldsymbol{X_1}$ contribute nonlinear restoration toward equilibrium, activated

415   respectively by shoreline and sandbar velocities. Their effect is complemented by the mixed interaction term $-a_{10}V_1V_3\boldsymbol{X_1}$,

which modulates shoreline forcing depending on the relative phases of shoreline and bar motion.

In contrast, the sandbar dynamics are dominated by two nonlinear amplification terms. The cubic component $+c_1X_3^2\boldsymbol{X_3}$

reflects an intrinsic instability of the sandbar, promoting large offshore or onshore excursions, while the term $+c_3X_1^2\boldsymbol{X_1}$

shows that the sandbar responds to large shoreline displacements with a similarly directed migration. Together, these terms

420   reveal a highly mobile system in which shoreline and sandbar motions interact through strongly nonlinear, velocity-modulated

feedbacks indicative of strong complexity where the typical equilibrium beach model may not be sufficient to effectively capture the beach temporal scales dynamics.

3.2.5 Synthesis: typology of shoreline–sandbar coupling

Despite their contrasting morphodynamic contexts, the three sites (Torrey Pines, Gold Coast, and Ensenada) share a common
425 structural backbone. (1) At all locations, the shoreline dynamics include a cubic restoring term $(-a_i X_1^2 \boldsymbol{X_1})$ that provides intrinsic stability for large excursions, indicating that the dominant component of shoreline variability is its seasonal response to changes in wave climate. This shared behavior is clearly visible in Fig. 6, where the fluence diagrams for all sites show a strong shoreline self-restoring loop, consistent with a common annual-cycle–controlled oscillation.

(2) The analysis further reveals that GPoM effectively captures the sandbar–shoreline morphological feedback loops. Al-
430 though the underlying monomials differ from site to site, their dynamical interpretation is remarkably consistent: the strength and sign of the feedback depend on the relative position of the sandbar with respect to the shoreline, reflecting the degree of wave-energy buffering exerted by the bar. In all systems, a sandbar located closer to the shoreline tends to reduce shoreline mobility, while large bar excursions increase the effective forcing reaching the shoreline.

(3) Shared shoreline–sandbar co-evolution mechanisms, although not captured in their full generality through the GPoM
435 framework, depend strongly on the timescale considered. This highlights that the system's integrated response may differ significantly from the instantaneous forcing. For example, Torrey Pines and Ensenada act as systems whose dissipation length adjusts to wave climate by moving from both ends of the surf zone (near similar feedback loops in the fluence diagrams within Fig. 6), whereas Gold Coast exhibits a translation-dominated behavior in which the surf-zone geometry is preserved as the entire system shifts seasonally. In addition, GPoM identifies enhanced dynamical complexity at Ensenada: the sign of the
440 shoreline–sandbar correlation depends on the rate of shoreline motion. During rapid shoreline disturbances (e.g. erosive coastal storm), the correlation may invert, leading the shoreline and sandbar to migrate in the same direction. This underscores the critical importance of the timescales used to model beach-profile evolution with physics-simplified approaches. The absence of such short-timescale reversals in the GPoM models of Torrey Pines and Gold Coast does not imply their non-existence. Indeed, the phase planes (X_1, X_3) in Fig. 3 show that short-lived reversals of the typical seasonal correlation are observed in the data
445 at these two sites as well.

Duck presents a fully distinct dynamical regime. Its shoreline dynamics are governed exclusively by nonlinear velocity-dependent interactions, with no autonomous restoring or destabilizing term acting directly on shoreline position. Sandbar–shoreline feedbacks become effective only when either the shoreline or the sandbar moves rapidly, while quadratic damping ensures substantial dissipation during energetic events. In contrast, the sandbar dynamics are driven by two nonlinear ampli-
450 fication terms (one intrinsic $(+c_1 X_3^2 \boldsymbol{X_3})$, the other associated with large shoreline excursions $(+c_3 X_1^2 \boldsymbol{X_1})$) revealing a highly mobile bar system subject to strong nonlinear forcing. This fully nonlinear, velocity-modulated regime is evident in Fig. 6, where Duck displays almost exclusively nonlinear feedback loops with little or no linear structure, suggesting that Duck Beach integrates several forcings acting over multiple timescales while exhibiting a rich internal dynamics. Altogether, this makes Duck the most complex system of the four, not adequately described solely through its response to wave forcing.
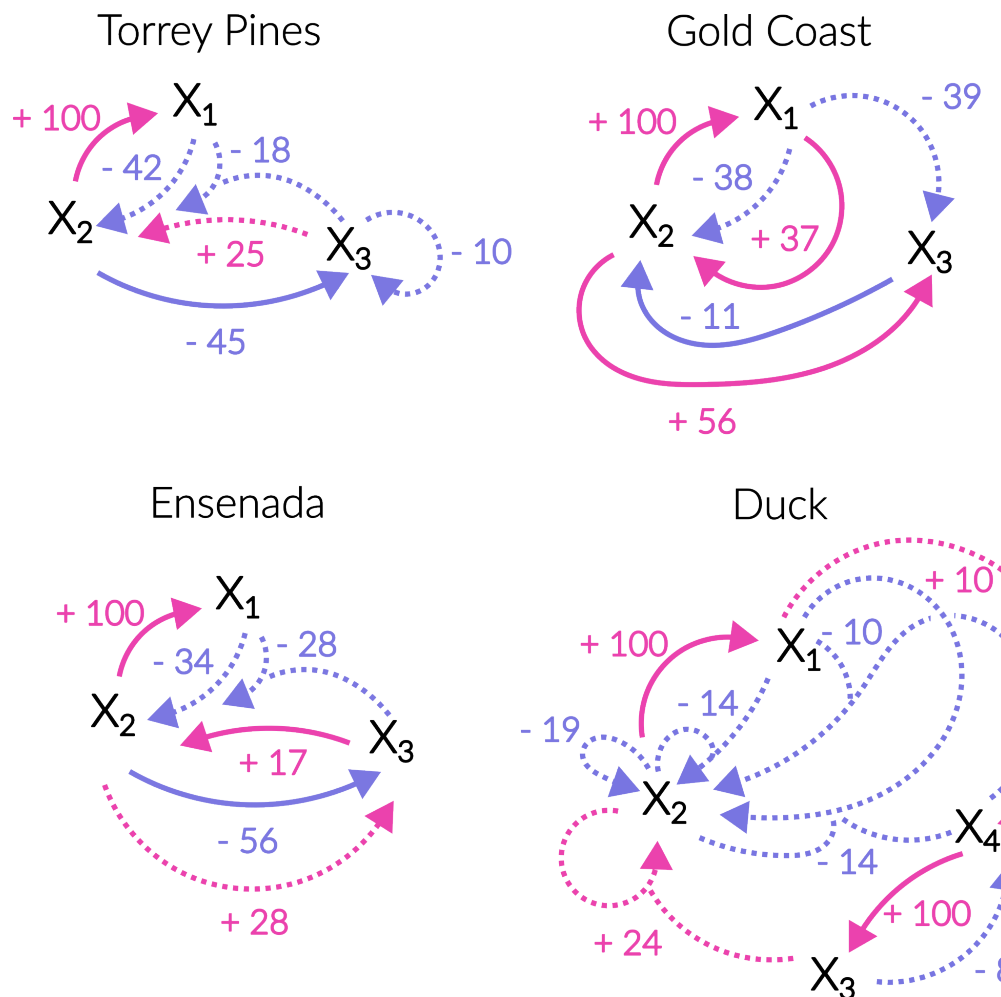
Figure 6. Fluence diagrams between the variables for the four sites. Fluence diagrams are presented to map the underlying positive (pink) and negative (light blue) feedback loops between variables, whether linear (solid lines) or nonlinear (dashed lines). The strength and sign of the feedback influence is derived directly from the variance explained by each term within its equation (Table 2-5) and the sign of the associated coefficient (Table1), respectively. Only terms accounting for 10% or more of the signal variability are considered.

Table 1. Models' coefficient weights comparison for the four sites of study.

Coefficient	Torrey Pines	Gold Coast	Ensenada	Duck
a_1	-2.95×10^{-4}	-3.89×10^{-4}	2.22×10^{-4}	-1.92×10^{-2}
a_2	2.69×10^{-4}	2.51×10^{-4}	-7.65×10^{-5}	7.73×10^{-3}
a_3	6.09×10^{-3}	1.08×10^{-2}	5.68×10^{-3}	3.31×10^{-1}
a_4	2.30×10^{-1}	4.81×10^{-1}	8.78×10^{-3}	4.56×10^{-1}
a_5	-1.62×10^{-4}	3.53×10^{-4}	-6.01×10^{-3}	-0.528×10^{1}
a_6	-2.79×10^{-4}	-3.50×10^{-4}	-1.92×10^{-4}	-6.32×10^{-4}
a_7	-2.24×10^{-4}	-8.95×10^{-1}	-5.97×10^{-3}	1.20×10^{-2}
a_8	—	1.45×10^{-4}	-1.16×10^{-4}	-3.48×10^{-1}
a_9	—	-2.13×10^{-4}	—	1.39×10^{-2}
a_{10}	—	—	—	-5.32×10^{-1}
a_{11}	—	—	—	-3.44×10^{-1}
a_{12}	—	—	—	2.07×10^{-4}
a_{13}	—	—	—	-6.07×10^{-5}
b_1	4.78×10^{-3}	6.27×10^{-3}	1.08×10^{-3}	—
b_2	7.25×10^{-3}	-2.01×10^{-3}	-3.43×10^{-3}	—
b_3	-7.94×10^{-1}	5.35×10^{-1}	-9.76×10^{-1}	—
b_4	-4.25×10^{-3}	-3.43×10^{-1}	3.61×10^{2}	—
b_5	-1.81×10^{-1}	-6.52×10^{-3}	1.40×10^{-3}	—
b_6	-1.69×10^{1}	—	2.35×10^{-3}	—
b_7	-1.42×10^{1}	—	1.22×10^{-3}	—
b_8	4.46×10^{-3}	—	—	—
b_9	-5.16×10^{-1}	—	—	—
b_{10}	-0.65×10^{1}	—	—	—
b_{11}	-1.39×10^{-1}	—	—	—
c_1	—	—	—	-2.92×10^{-4}
c_2	—	—	—	-1.23×10^{-2}
c_3	—	—	—	9.82×10^{-5}

Table 2. Analysis of variance of the GPoM model – site of **Torrey Pines**. The variances are normalized by equation (Var_{eq}) and at the scale of the entire model ($\text{Var}_{\text{global}}$).

Equation	Sign	Coeff.	Term	Var_{eq}
$\dot{X}_1$	+	1	X_2	1.00000
	−	a_7	X_1^3	0.41562
	+	a_2	X_3^3	0.25180
	−	a_6	$X_1^2 X_3$	0.17950
$\dot{X}_2$	−	a_1	X_3	0.08843
	−	a_5	$X_1 X_3^2$	0.03247
	+	a_3	$X_2 X_3^2$	0.01936
	+	a_4	$X_2^2 X_3$	0.01283
	−	b_3	X_2	0.44985
	−	b_4	X_3^3	0.10373
	−	b_9	$X_1 X_2 X_3$	0.09210
	+	b_2	X_3	0.08788
$\dot{X}_3$	−	b_7	$X_2^2 X_3$	0.08075
	−	b_6	X_2^2	0.07506
	+	b_8	X_1	0.04886
	−	b_5	$X_2 X_3^2$	0.02817
	−	b_{11}	$X_1^2 X_2$	0.02005
	−	b_{10}	$X_1 X_2^2$	0.01356

Table 3. Analysis of variance of the GPoM model – site of Gold Coast. The variances are normalized by equation (Var_{eq}) and at the scale of the entire model ($\text{Var}_{\text{global}}$).

Equation	Sign	Coeff.	Term	Var_{eq}
$\dot{X}_1$	$+$	1	X_2	1.00000
	$-$	a_9	X_1^3	0.38335
	$+$	a_5	X_1	0.36809
	$-$	a_1	X_3	0.10747
	$-$	a_7	$X_1 X_2^2$	0.04760
$\dot{X}_2$	$-$	a_6	$X_1 X_3^2$	0.04014
	$+$	a_8	$X_1^2 X_3$	0.02308
	$+$	a_3	$X_2 X_3$	0.01149
	$+$	a_2	X_3^3	0.01135
	$+$	a_4	$X_2^2 X_3$	0.00743
	$+$	b_3	X_2	0.56438
$\dot{X}_3$	$-$	b_5	X_1^2	0.38997
	$-$	b_4	$X_2 X_3^2$	0.03071
	$-$	b_2	X_3	0.01495

Table 4. Analysis of variance of the GPoM model – site of **Ensenada**. The variances are normalized by equation ($\mathrm{Var_{eq}}$) and at the scale of the entire model ($\mathrm{Var_{global}}$).

Equation	Sign	Coeff.	Term	$\mathbf{Var_{eq}}$
$\dot{X}_1$	+	1	X_2	1.00000
	−	a_8	X_1^3	0.33919
	−	a_6	$X_1^2 X_3$	0.27605
	+	a_1	X_3	0.17264
$\dot{X}_2$	−	a_7	$X_1^2 X_2$	0.06371
	−	a_2	$X_1 X_3^2$	0.05920
	+	a_4	$X_1 X_2$	0.04883
	−	a_5	$X_1 X_2 X_3$	0.02393
	+	a_3	X_2	0.01645
	−	b_3	X_2	0.56105
	+	b_4	X_2^3	0.27808
$\dot{X}_3$	+	b_6	$X_1^2 X_3$	0.04767
	−	b_2	X_3	0.04744
	+	b_7	X_1^3	0.04288
	+	b_5	$X_1 X_3^2$	0.02288

Table 5. Analysis of variance of the GPoM model – site of **Duck**. The variances are normalized by equation ($\mathrm{Var_{eq}}$) and at the scale of the entire model ($\mathrm{Var_{global}}$).

Equation	Sign	Coeff.	Term	$\mathrm{Var_{eq}}$
$\dot{X}_1$	+	1	X_2	1.00000
	+	a_4	$X_2^2 X_3$	0.24364
	−	a_5	X_2^3	0.19205
	−	a_{10}	$X_1 X_2 X_4$	0.14097
	−	a_{11}	$X_1 X_2^2$	0.13808
	−	a_8	$X_1 X_4^2$	0.10359
	+	a_2	$X_3^2 X_4$	0.06405
$\dot{X}_2$	−	a_1	X_4	0.02660
	+	a_9	$X_1 X_2$	0.02105
	+	a_3	$X_2 X_4$	0.01964
	−	a_6	X_1	0.01906
	+	a_7	$X_1 X_4$	0.01385
	−	a_{13}	X_1^3	0.00892
	+	a_{12}	X_1^2	0.00850
$\dot{X}_3$	+	1	X_4	1.00000
	−	c_1	X_3^3	0.82360
$\dot{X}_4$	−	c_3	X_1^3	0.10312
	+	c_2	$X_1 X_2$	0.07328

3.3 Chaos within shoreline–sandbar systems

To exhibit chaos, a dynamical system must be – at the same time – deterministic, highly sensitive to the initial conditions and bounded. Several properties then follow from these necessary conditions (Bergé et al., 1986; Letellier et al., 2021). Dynamically, the time evolution of the system becomes unpredictable in the long term (Wolf et al., 1985; Grond et al., 2003); geometrically, the trajectories evolve on an attractor with fractal geometry (Ruelle, 1976; Ott, 2002; Grassberger and Procaccia, 1983); and topologically, the structure of this attractor involves stretching and folding mechanisms (Gilmore and Lefranc, 2002). Various tools have been developed to detect these conditions and properties, although they come with limitations and

impose constraints on both the formulations and the data (Eckmann and Ruelle, 1992; Ding et al., 1993). In all cases, proving that the system is deterministic remains a necessary condition for which only a few tools exist when working with real-world observational datasets.

465   In natural systems, the aforementioned requirements for chaos to emerge are rarely met simultaneously, which makes direct evidence of such dynamics elusive. The GPoM framework bridges this gap by reconstructing explicit deterministic equations directly from observational time series, thus revealing the underlying coupling structure. This approach provides the missing link between empirical observations and theoretical determinism, allowing the full dynamical characterization of coastal morphodynamics. Extracting validated equations directly from observed time series allows one to obtain all the necessary

470   conditions and properties of chaos within a consistent framework. Determinism is guaranteed by the reconstructed equations, which converge to an attractor, and their robustness can be checked numerically. These equations also enable a direct computation of Lyapunov exponents (λ_i) and attractor dimensions via the corresponding Kaplan–Yorke dimension (D_{KY}), offering a rigorous diagnostic of chaos from real-world data. Similarly, topological properties can also be deduced from it.

The Lyapunov spectrum $\{\lambda_i\}$ was estimated numerically following the Benettin algorithm, adapted to the GPoM frame-

475   work (Benettin et al., 1980). The reconstructed models were integrated over long synthetic trajectories using a fourth-order Runge–Kutta scheme. The local tangent flow was estimated by finite differences of the flow map $\Phi_h(\mathbf{X})$, and an orthonormal basis of perturbations was propagated and reorthonormalized at each step using a QR decomposition (Gander, 1980). The Lyapunov exponents were then obtained as the time-averaged logarithms of the diagonal elements of the R matrix:

$$\lambda_i = \frac{1}{N\,\Delta t}\sum_{k=1}^{N}\log|R_{k,ii}|. \tag{13}$$

480   The Kaplan–Yorke dimension (Kaplan and Yorke, 1979) was obtained as:

$$D_{KY} = j + \frac{\sum_{i=1}^{j}\lambda_i}{|\lambda_{j+1}|}, \quad \text{where } j = \max\left\{n : \sum_{i=1}^{n}\lambda_i > 0\right\}. \tag{14}$$

All calculations were performed on the numerically integrated models after transient removal. The leading Lyapunov exponents ($\lambda_1 > 0$) confirm that all four systems present a high sensitivity to the initial conditions which – associated with the determinism guarantied by the obtained equations – provides a first argument for chaos (Table 6). This implies finite predictabil-

485   ity horizons on the order of months to years, in line with observed study sites shoreline–sandbar main variability. The total divergence ($\sum_i \lambda_i < 0$) indicates that the systems remain globally dissipative, with attractor contraction typical of bounded physical processes.

The non-integer values of the Kaplan–Yorke dimensions ([2.3–2.8]) confirm the fractal nature of these attractors, implying scale-invariant structures and self-similar organization within the coupled shoreline–sandbar dynamics, and provide another

490   argument for chaos. The dimensions obtained here are all quite high compared with the strongly dissipative chaos commonly observed in systems such as the paradigmatic Lorenz-1963 or Rössler-1976 models, whose dimension does not exceed 2.06. Very few continuous systems with fractal dimension greater than 2.10 were identified in the early development of chaos,

whose lower dissipation gives them a characteristic foliated structure (Lorenz, 1984; Langford, 1984). From this perspective, the results obtained here are of particular interest because they confirm that this type of dynamics can also be extracted directly from real-world observational data.

Table 6. Lyapunov exponents, divergence, Kaplan–Yorke dimension and Horizons of Predictability (HP) for the autonomous GPoM models identified at each site. Positive λ_1 indicates sensitivity to initial conditions, near zero λ_2 correspond to the direction of the flow, negative λ_3 reflect energy dissipation (i.e. attractor boundedness) while $\sum_i \lambda_i$ measures the system divergence. The deterministic horizon (HP_σ) corresponds to the time when the mean RMS error equals the natural variability (1σ), here typically on semi-annual scales, indicating that the model retains the large-scale seasonal shoreline–sandbar dynamics. In contrast, the probabilistic horizon ($HP_{25\%,90\%}$) marks the time when 90% of runs exceed a 25% relative error, revealing rapid trajectory divergence and high sensitivity to initial conditions. Together, they show that the models preserve the global morphodynamic structure but offers forecasting ability at short time scale, as, the annual forcing imprint remain consequent within the morphological evolutions.

Site	λ_1	λ_2	λ_3	λ_4	D_{KY}	HP_σ	$HP_{25\%,90\%}$
	[day^{-1}]	[day^{-1}]	[day^{-1}]	[day^{-1}]	[–]	[days]	[days]
Torrey Pines	$(1.0 \pm 1.1) \times 10^{-3}$	$(2.4 \pm 1.1) \times 10^{-4}$	$(-3.4 \pm 1.9) \times 10^{-3}$	—	2.310 ± 0.139	167	25
Gold Coast	$(3.4 \pm 0.53) \times 10^{-3}$	$(1.7 \pm 1.2) \times 10^{-3}$	$(-7.0 \pm 1.7) \times 10^{-3}$	—	2.731 ± 0.198	173	32
Ensenada	$(2.4 \pm 1.9) \times 10^{-3}$	$(6.9 \pm 14.0) \times 10^{-4}$	$(-4.5 \pm 1.9) \times 10^{-3}$	—	2.408 ± 0.920	241	29
Duck	$(3.5 \pm 1.8) \times 10^{-3}$	$(1.4 \pm 1.5) \times 10^{-3}$	$(-5.3 \pm 2.3) \times 10^{-3}$	$(-2.0 \pm 0.6) \times 10^{-2}$	2.846 ± 0.304	112	17

To analyze the organization of the reconstructed attractors, Poincaré sections were extracted; from which first return maps were computed (Fig. 7.a-c). Within the figure, each point corresponds to a successive intersection of the trajectory with the section, producing a discrete sampling of the continuous flow. This representation highlights how the flow stretches, folds, and squeezes from one passage to the next, making the underlying invariant structure directly visible. For a basic periodic orbit, the section would collapse into a single point, while quasi-periodic dynamics would produce a smooth closed curve. In contrast, deterministic chaos yields discontinuous but characteristic structured patterns of points. In the most common case, this organization can take an inverted-U shape crossing the median, as is the case for the logistic map (May, 1976), reflecting a single folding process that generates two distinct branches from a single branch at each iteration. More branches may be generated, leading to a multimodal distribution of points with multiple crossings of the median. Some situations may require several Poincaré sections of the same attractor to obtain a proper map-based description of the underlying structure. Branches may be clearly visible under strongly dissipative conditions, in which each branch corresponds to a single line, but are more difficult to depict under weakly dissipative conditions (as is the case here), because each branch can exhibit a thick, foliated structure.
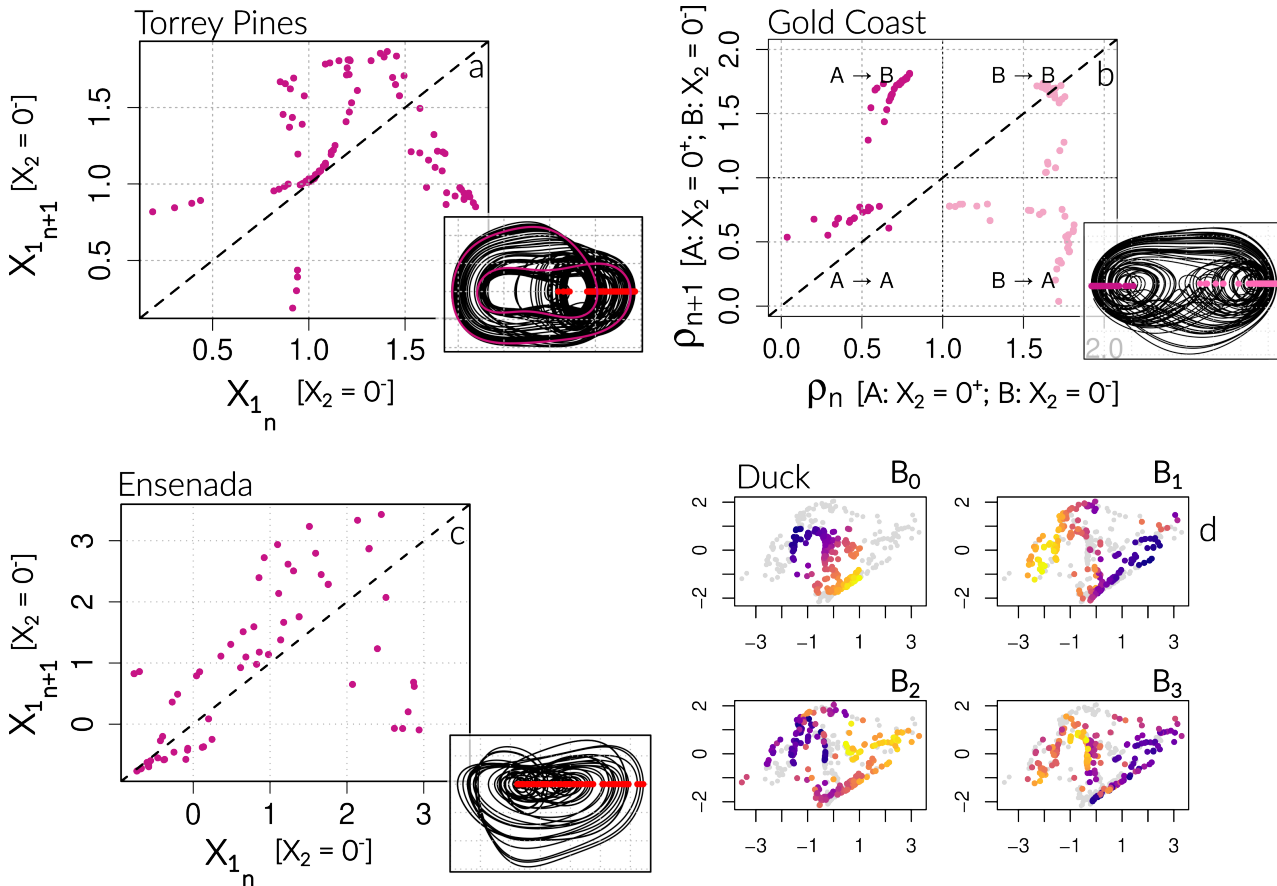
Figure 7. First-return maps or Poincaré sections computed for the four reconstructed systems. (a–c) Each dot corresponds to a successive intersection of the trajectory with the Poincaré section, providing a discrete sampling of the underlying continuous flow. The corresponding Poincaré section is overlaid (red dots for Torrey Pines and Ensenada, shade of pink for Gold Coast) on a two-dimensional representation of each attractor within each subpanel. (a) First-return map computed by applying dynamical noise during model integration in order to prevent the trajectory from falling into the period-2 basin normally reached in case of noise-free run (pink cycle within the subpanel). (b) First-return map computed for two distinct branches of the attractor (branch A: dark pink; branch B: light pink). (d) Poincaré section projected onto the (X_1, X_3) plane. B_0 denotes the initial neighborhood selected within the section, and B_i ($i = 1, 2, 3$) its successive images under the first-return map. Because the reconstructed Duck attractor has four embedding dimensions, colored markers are used to track the deformation and transport of B_0 across iterations, allowing the local geometry of the attractor to be visualized despite the two-dimensional projection.

At Torrey Pines, the trajectory was found to converge toward a stable period-two orbit after a very long transient. The compli-
510 cated dynamics observed in the model phase portraits (Fig. 3) is therefore only metastable, although it may be easily triggered by perturbations. Since the Lyapunov exponents and the Kaplan-Yorke dimension ($D_{KY} \approx 2.31$, see Table 6) were estimated over this transient and thus characterize the associated dynamics, corresponding to metastable, weakly dissipative chaos. In

order to represent the structure of this metastable transient, the first-return map was constructed by adding dynamical noise ($\epsilon = 10^{-5} \times \sigma_{X_1}$, with σ_{X_1} the standard deviation of the variable X_1) during model integration to prevent the trajectory from

515 falling into the stable periodic orbit obtained in the noise-free integration case; enabling to reveal the underlying deterministic structure (Fig. 7.a). The resulting map clearly exhibits a structure with an inverted-U shape characteristic of chaos. Its foliation reveals the folding of at least two main branches, possibly more.

At Gold Coast, the attractor is organized inside a genus-3 torus, which requires defining two Poincaré sections for a proper description (Rosalie and Letellier, 2014). The two sections were defined on the surface $X_2 = 0$ (see Fig. 7.b): the left one

520 (A), on the interval $X_1 \in [-2, -0.5]$, corresponding to a positive crossing ($X_2 = 0^+$), and the right one (B), on the interval $X_1 \in [0, 2]$, corresponding to a negative crossing ($X_2 = 0^-$). To reconstruct the first-return map, these two sections were assembled using a single coordinate axis. A decreasing orientation was defined for section A as: $\rho_A = (-0.5 - X_1)/(1.5)$, while an increasing orientation was defined for section B as: $\rho_B = 1 + X_1/2$, yielding a unified return interval $\rho \in [0, 2]$. The global return map $\rho_{n+1} = \mathcal{P}(\rho_n)$ thus explicitly resolves transitions within and between the different parts of the attractor, with

525 the four quadrants of the map corresponding to A→A; A→B; B→A and B→B transitions. In agreement with the organization of the attractor observed in phase space (Fig. 3), the map confirms the presence of the four possible transitions (A→A; A→B; B→A; and B→B), indicating that the dynamics recurrently explores both parts of the attractor. The double-slash shape observed in the A→B region corresponds to a three-branch folding structure, but here with the middle branch missing.

At Ensenada, the first-return map (Fig. 7.c) is organized along a foliated bend revealing at least two distinct folding branches

530 that provide a strong argument for chaos. The foliated structure is characteristic of a weakly dissipative chaotic attractor ($D_{KY} = 2.4$). The attractor involves an extremely thin central branch on which all the trajectories loop at the bottom and pass through the attractor before reemerging and separating at the top (Fig. 3). This structure is similar to the 'cord attractor' discovered in 2011 (Letellier and Aguirre, 2012), although here the thin central cord is completely bent within the attractor, which may make the detailed analysis of this attractor's structure particularly challenging.

535 The case of Duck is even more demanding. Indeed, analyzing the structure of chaotic attractors becomes a hard problem when their dimension is larger than three (Gilmore and Lefranc, 2002; Letellier and Gilmore, 2013). Few techniques have been developed to investigate their structure (Mindlin and Gilmore, 1992; Gilmore and Lefranc, 2002; Mangiarotti et al., 2014). Recently, promising results have been obtained based on homology (Charó et al., 2021; Sciamarella and Charó, 2024), but their application remains difficult in many cases. Developed to characterize foliated structures, color tracer mapping can be

540 an alternative, in particular because it can also be applied to toroidal chaos and to four-dimensional problems (Rosalie and Mangiarotti, 2025; Mangiarotti et al., 2023). This technique consists of applying color tracers at a chosen Poincaré section and examining their reorganization between successive iterations. The tracers allow one to follow the evolution of a small neighborhood of points across successive returns. This technique was applied to investigate the presence of folding and stretching within the Poincaré section of the Duck attractor (Fig. 7.d), which is very thick as consistently shown by an estimated dimen-

545 sion close to three ($D_{KY} = 2.85$). Starting from an initial state B_0, points are first selected within a compact region of the Poincaré section and colored according to their position along the first principal component obtained from a local PCA. This color assignment provides a continuous label that allows tracking the deformation of a small neighborhood under successive

returns of the dynamics. The images of B_0 at successive states B_1, B_2, and B_3 reveal (1) very strong stretching: initially confined to a localized region in B_0, the colors spread over almost the entire Poincaré section after a single iteration (B_1); (2) strong mixing, since after several iterations, points carrying very distant colors in B_0 come into contact in B_3. This behavior results from the combined action of folding (where the color gradient remains locally consistent almost everywhere between successive iterations, as illustrated in B_1), and squeezing, evidenced by the local compaction of trajectories in specific regions of the section.

Together with the positive first Lyapunov exponent and the fractal dimension, and supported by the deterministic nature guaranteed by the reconstructed equations, the first-return maps and the color tracer mapping provide dynamical, geometrical, and topological evidence of weakly dissipative chaos at the four sites either as a transient dynamics recurrently triggered by external forcing (Torrey Pines) or as permanent dynamics (at the other three sites). This implies that shoreline–sandbar systems exhibit chaos-prone internal dynamics associated with energy dissipation mechanisms and morphodynamic feedback loops, but this dissipation remains weak compared to the energy inputs (i.e., forcings). Therefore, this system is not strongly damped, a marker of long-term memory and sensitivity to small perturbations.

The bifurcation diagrams (Fig. 8), obtained by slowly varying the coefficient values of specific terms, were also reconstructed. They present contrasted behaviors over the studied sites. The classical doubling period cascade was not observed at any of them, which may be an indication of toroidal chaos, as observed in low-dimensional models of atmosphere dynamics.
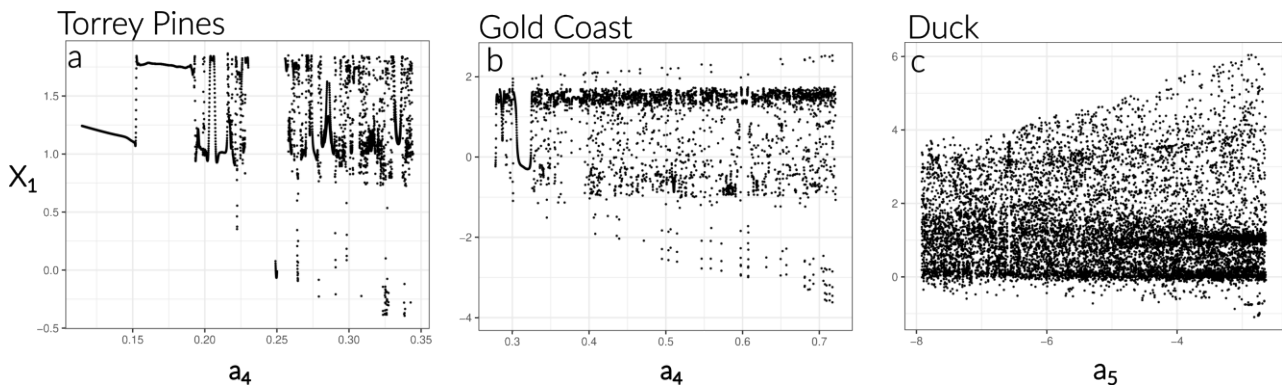
Figure 8. X_1 **bifurcation diagram for three of the four sites.** (a-b) Torrey Pines and Gold Coast for the term $a_4 X_2^2 X_3$ and (c) Duck for the term $a_5 X_2^3$ within the $\dot{X}_2$ equation when varying a_i from 0.5 to 1.5 times its original value for 5000 runs over 10 years. The X_1 local maxima over the last 300 days of each run are then scattered. For Gold Coast and Duck, transients have been removed, whereas the stable regime at Torrey Pines takes approximately ten years to be established; consequently, its bifurcation diagram explores the complexity of the transient dynamics.

At Torrey Pines, the bifurcation diagram is characterized by abrupt alternation of periodic, either period-1 (single value e.g. at $0.11 < a_4 < 0.18$ with an abrupt change of amplitude at $a_4 = 0.155$), or more rarely period-2 (two values e.g. at $0.28 < a_4 < 0.29$) dynamics, and chaotic (complex distribution of points, in the ranges $[0.21; 0.22]$, $[0.26; 0.27]$, $[0.31; 0.33]$) and organized around two main regions: around $X_1 = 1.25$ and $X_1 \in [1.0; 1.25]$. An organization around two main layers is also

observed at Gold Coast, but the dynamic appears periodic only in very localized regions (e.g. in $0.3 < a_4 < 0.32$) whereas the dynamic is chaotic elsewhere. The bifurcation diagram could not be reconstructed at Ensenada, indicating that the inferred

570 dynamics is quite specific to the parameterization. Finally, at Duck, the dynamic was found chaotic on the whole parameter window ($-7.8 < a_5 < -2.5$). Because the model obtained at this site is four-dimensional, the very high value of D_{KY} suggest a proximity to hyperchaos, which requires two positive Lyapunov exponents ($\lambda_1 > \lambda_2 > \lambda_3 = 0 \gg \lambda_4$), (Rössler, 1979, 1983).
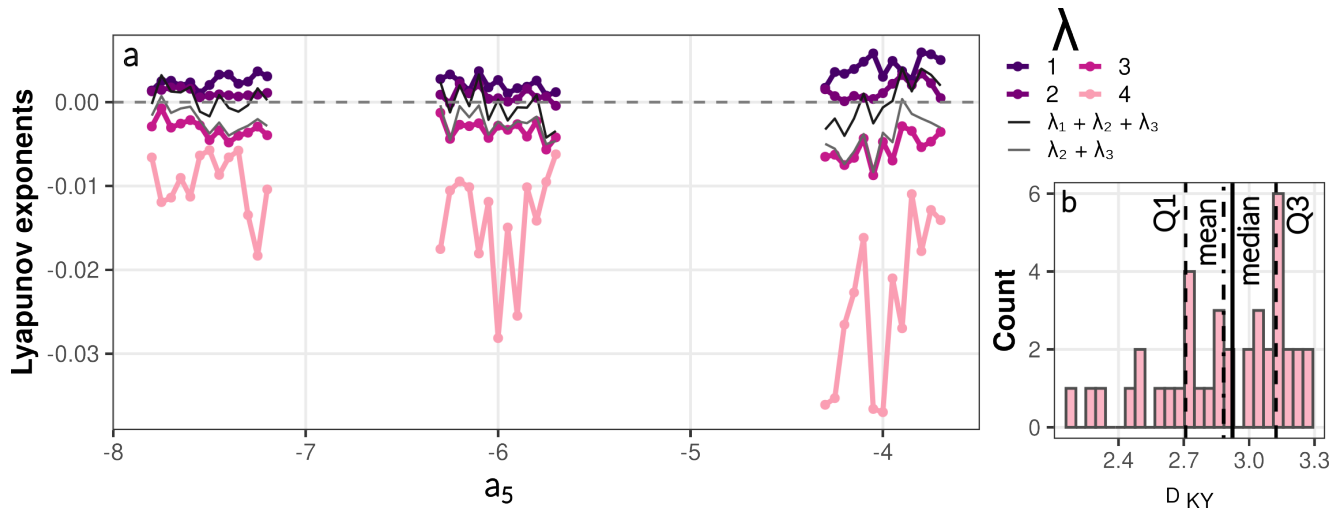
Figure 9. Lyapunov analysis of Duck as a function of various ranges of the control parameter a_5**.** (a) Lyapunov spectrum estimated after transient removal. Thin black and gray lines show the sums $\lambda_2 + \lambda_3$ and $\lambda_1 + \lambda_2 + \lambda_3$, used to diagnose the proximity to a regime with two expanding directions and to highlight regions of weak dissipation, respectively. (b) Distribution of the Kaplan–Yorke dimension D_{KY} computed from the Lyapunov spectrum for all tested values of a_5. The dimension predominantly lies between approximately 2.7 and 3.3, with a median value close to 3.

To investigate this question, the Lyapunov spectrum was estimated in three subwindows of the bifurcation diagram, around $a_4 = 7.75$, -6, and -3.9. Fig. 9.a shows the individual Lyapunov exponents of the Duck system as a function of the control

575 parameter a_5 after transient removal. The largest exponent λ_1 is strictly positive over the entire parameter range, indicating robust chaotic dynamics. The second exponent λ_2 remains close to zero almost everywhere and significantly smaller than λ_1, while λ_3 and λ_4 are negative. In continuous autonomous systems, one Lyapunov exponent must equal zero, corresponding to the direction of the flow. Since numerical algorithms do not explicitly isolate this direction, the neutral exponent may be mixed with nearby weakly stable or unstable directions. As a result, particular care must be taken when interpreting a second small

580 positive exponent as evidence for hyperchaos. To address this issue, we additionally show the sums $\lambda_2 + \lambda_3$ and $\lambda_1 + \lambda_2 + \lambda_3$. Negative values of $\lambda_2 + \lambda_3$ are obtained almost everywhere indicating that λ_2 is closer to zero and corresponds to the flow direction ($\lambda_2 \equiv 0$). Positive values of $\lambda_2 + \lambda_3$ indicate λ_3 is closer to zero and corresponds to the flow direction ($\lambda_3 \equiv 0$). The former condition is observed almost everywhere while the latter one is observed only very locally in parameter space ($a_5 = -7.75$ and -3.9), suggesting that the dynamical system may reach hyperchaotic regimes under small configuration

585   changes and that, overall, the observed dynamics operates close to hyperchaos. The partial sum $\lambda_1 + \lambda_2 + \lambda_3$ provides an estimate of the effective dissipation and highlights parameter regions where the dynamics is weakly dissipative. As shown, this sum is often close to or above zero for the explored parameter values, supporting the interpretation of a low-dimensional, weakly dissipative chaotic attractor. The associated D_{KY} distribution mostly lies between 2.7 and 3.3 (Fig. 9.b), with a median value close to 3. While $D_{KY} > 3$ is not sufficient to establish hyperchaos, it provides geometric support for the interpretation

590   that the Duck system operates near the transition between chaotic and hyperchaotic regimes. To conclude, the Duck system exhibits robust chaos across the explored parameter range and displays signatures consistent with proximity to hyperchaotic dynamics, although the identification of a fully developed hyperchaotic regime is limited to narrow regions of parameter space.

In addition, the predictability horizons (HP) were evaluated (Table 6) from the growth of the prediction error over an ensemble of 50 initial conditions using two complementary criteria (See Supplementary material Fig. S1-12). The first, HP_σ,

595   corresponds to the time at which the mean RMSE reaches one standard deviation of the observed signal, marking the loss of dynamical coherence between simulated and observed trajectories. The second, $HP_{25\%,90\%}$, follows the probabilistic approach proposed by Mangiarotti and Le Jean (2023), defined as the horizon at which 90% of the ensemble members exhibit a relative error exceeding 25% of the signal amplitude. Across sites, both criteria yield consistent results, with HP_σ typically of the order of half a year and $HP_{25\%,90\%}$ around one month. This dual structure of predictability indicates that the reconstructed models

600   retain short-term skill for about one monthly cycle, while maintaining partial dynamical consistency over the semi-annual timescale. The semi-annual predictability horizon is consistent with the dominant systems' annual periodicity, over which the autocorrelation of the principal morphological proxies of beach evolution remains significant for approximately half a cycle (Reeve et al., 2014). This suggests that the models reproduce the internal oscillatory memory of the system, while their forecast skill remains limited in the absence of external forcing driving the dynamics. Conversely, the shorter $HP_{25\%,90\%}$ reflects the

605   timescale beyond which small phase errors accumulate to produce significant amplitude mismatches, even though the overall trajectory remains within the correct attractor. Beyond their diagnostic value, these horizons also serve as a model validation metric: obtaining realistic, finite predictability horizons confirms that the reconstructed dynamics capture the intrinsic memory of the coastal system rather than overfitting the data.

Taken together, these results demonstrate that all four systems operate within a chaotic regime. First, the four dynamics can

610   be approximated by low-dimensional ordinary differential equations, which are a strong argument in favor of determinism and a necessary condition for chaos. The solutions of these equations converge toward attractors of nontrivial structure, characterized by a strong sensitivity to initial conditions ($\lambda_1 > 0$) and finite predictability (Table 6), which constitutes another necessary condition for chaos. The resulting attractors exhibit a fractal structure with single or multiple foldings, a hallmark of chaotic dynamics. More specifically, the attractors display a thick structure, a property rather rarely encountered in chaotic systems,

615   as reflected by their Kaplan–Yorke dimensions ($2.31 < D_{KY} < 2.85$). Such dynamics establish the bridge between short-term unpredictability and long-term structural coherence, consistent with the self-regulated nature of coastal morphodynamic systems driven by processes spanning a broad range of spatiotemporal scales, from storm events to climatic modulations.

4 Discussion

This study provides direct evidence that the coupled shoreline–sandbar system behaves as a low-dimensional deterministic
dynamical system across a wide range of morphodynamic settings. The ability of the reconstructed models to reproduce both
the geometry of the phase space and the multiscale spectral structure of the observations indicates that the essential dynamics
are captured by a small number of interacting degrees of freedom. This supports the view that sandy beaches, despite being
continuously forced by waves and other environmental variables, can organize their response through deterministic internal
dynamics. Importantly, the models are fully autonomous: no external forcing is prescribed, yet the reconstructed dynamics
retain realistic amplitudes, oscillatory behavior, and broadband red spectra. This implies that the influence of external drivers
is effectively embedded within the internal state variables, and that the shoreline–sandbar system integrates forcing over time
through its own nonlinear structure.

Across all sites, the reconstructed equations reveal that shoreline and sandbar dynamics are mutually coupled, rather than
hierarchically driven. The shoreline does not simply respond passively to sandbar migration, nor does the sandbar act as
an independent buffer; instead, both components participate in closed feedback loops whose strength and sign depend on
the system state. For Torrey Pines and Ensenada, the dominant coupling corresponds to a seasonal exchange mechanism in
which offshore sandbar migration accompanies shoreline retreat, while onshore migration promotes recovery. This behavior is
consistent with a variable surf-zone dissipation length that adapts to wave climate, producing bounded oscillations around a
stable mean state. At Gold Coast, the coupling differs qualitatively: shoreline and sandbar positions tend to evolve coherently,
indicating a translation-dominated regime in which the surf-zone geometry is conserved. The Duck system, operating within a
regime close to hyperchaos, departs markedly from the other sites. Its dynamics are dominated by velocity-dependent nonlinear
interactions, with no direct restoring term acting on shoreline position. Sandbar dynamics exhibit intrinsic instability and strong
sensitivity to shoreline motion, resulting in a highly complex attractor structure. This supports field-based interpretations of
Duck as a system with strong memory effects and path dependence, where antecedent morphology conditions subsequent
evolution (Anderson et al., 2023). These results indicate that shoreline–sandbar coupling is not universal in form, but universal
in presence: internal feedbacks are always active, yet their organization depends on the morphodynamic regime.

Therefore, relating these results to established coastal morphodynamic classifications (Wright and Short, 1984; Masselink
and Short, 1993; Castelle and Masselink, 2023) provides a consistent framework to draw implications from the present results.
The conclusion inferred here from the analysis of autonomous models derived from observational data shows that part of the
shoreline and sandbar variability should be interpreted as internally generated, rather than as a direct response to short-term
fluctuations in external forcings, even if their imprint on morphological evolution remains dominant at the seasonal scale. This
presents implications for both modeling and signal interpretation, since phenomena that are part of the internal dynamics of
sandy beaches (lags, feedback loops, morphodynamic turbulence, and so on) necessarily account for a non-negligible fraction
of the variability, which process-based models that neglect internal nonlinear feedbacks may misattribute to stochastic forcing
or parameter uncertainty. The low dimensionality of the reconstructed systems further implies that shoreline–sandbar dynamics
may be amenable to reduced-order modeling approaches that explicitly account for nonlinear coupling and instability, rather

than relying solely on equilibrium frameworks (Yates et al., 2009; Davidson et al., 2013; Dean, 1991). While the present models are not predictive tools for the long term, they provide a dynamical benchmark against which more complex models can be evaluated. Moreover, the existence of site-specific coupling structures suggests that coastal typologies based solely on external forcing or mean morphology may be incomplete. Internal dynamics and feedback organization appear to play a central role in controlling both variability and resilience of the beach system.

Finally, the estimated Lyapunov spectra imply finite predictability horizons, typically on the order of months to a few years, consistent with observed limits in shoreline forecasting skill. A recent large-scale benchmarking study have shown that shoreline prediction skill saturates at levels comparable to observational uncertainty, regardless of model complexity (Mao et al., 2025). While often attributed to data limitations, our results suggest that this saturation may also reflect an intrinsic loss of predictability associated with low-dimensional chaotic dynamics. This result provides a dynamical explanation for why long-term prediction of shoreline position remains challenging even when wave climate statistics are well characterized: beyond a certain horizon, forecast uncertainty grows exponentially due to internal instability, not because of incomplete forcing information. From this perspective, the shoreline–sandbar system behaves as a chaotic oscillator: its dynamics are structured and deterministic, yet long-term trajectories are inherently unpredictable. This reconciles the apparent contradiction between reproducible seasonal patterns and large interannual variability observed in many sandy beaches.

5 Conclusions

This study demonstrates that sandy shoreline–sandbar systems, despite strong environmental variability, can be represented by low-dimensional deterministic models exhibiting chaotic dynamics. Using global polynomial modeling applied to multi-year satellite-derived observations, we reconstructed autonomous equations that reproduce the essential coupling between shoreline and sandbar motion. The models reveal bounded, chaotic attractors with finite predictability horizons, highlighting the coexistence of short-term irregularity and long-term structural organization.

Across sites, the nonlinear feedbacks controlling shoreline acceleration and sandbar migration define distinct regimes (from dissipative to intermittently unstable oscillators) governed by the sign and strength of sandbar-related coupling terms. The emergence of chaos thus reflects an intrinsic property of morphodynamic systems where energy exchanges between shoreline and sandbar sustain self-regulated variability.

Despite these advances, several limitations remain. The GPoM framework relies on empirical reconstruction and is therefore dependent on the observed variables and time series used for the analysis. Moreover, it does not explicitly resolve physical processes such as sediment transport or hydrodynamics. Furthermore, the contribution of external forcing is not explicitly considered in this study. Temporal sampling and noise in satellite observations also constrain the precision of model coefficients and Lyapunov estimates. Furthermore, the analysis is restricted to 3–4-dimensional systems, which may overlook higher-order or non-local interactions present in real coastal dynamics.

Future work should focus on coupling autonomous data-driven dynamical reconstruction and climate forcing to assess how external variability (waves, storms, sea-level rise) interacts with intrinsic shoreline–sandbar dynamics. Expanding the analysis 685 to other coastal settings would help assess for the variety of these nonlinear behaviors.

Overall, this study provides a novel dynamical framework to interpret shoreline evolution as a self-regulated, chaotic system. It bridges satellite observation and system dynamics theory, offering new tools to assess the stability, predictability, and resilience of sandy coasts under changing environmental conditions.

Appendix A: Model simplification details

A1 Torrey Pines

Considering only the terms with a variance of $Var_{eq} \geq 10\%$ (see Table 2) leads to:

$$
\begin{cases}
\dot{X}_1 = X_2 \\
\dot{X}_2 = -a_7 X_1^3 + a_3 X_2^3 - a_6 X_1^2 X_3 \\
\dot{X}_3 = -b_3 X_2 - b_4 X_3^3.
\end{cases}
\tag{A1}
$$

Defining the second order derivatives, we get:

$$
\begin{cases}
\ddot{X}_1 = -a_7 X_1^3 + a_2 X_3^3 - a_6 X_1^2 X_3 \\
\ddot{X}_3 = -b_3 \ddot{X}_1 - 3b_4 X_3^2 \dot{X}_3,
\end{cases}
\tag{A2}
$$

and then:

$$
\begin{cases}
\boldsymbol{A}_1 = -a_7 X_1^2 \boldsymbol{X}_1 + a_2 X_3^2 \boldsymbol{X}_3 - a_6 X_1^2 \boldsymbol{X}_3 \\
\boldsymbol{A}_3 = -b_3 \boldsymbol{A}_1 - 3b_4 X_3^2 \boldsymbol{V}_3,
\end{cases}
\tag{A3}
$$

with $\boldsymbol{A_i}$ and $\boldsymbol{V_i}$ the sand mass acceleration and speed, respectively. Under the hypothesis that both masses are equal ($m_1 = m_3$), we can view the problem as the force applied to the sand masses as:

$$
\begin{cases}
\boldsymbol{F}_1 = -a_7 X_1^2 \boldsymbol{X}_1 + a_2 X_3^2 \boldsymbol{X}_3 - a_6 X_1^2 \boldsymbol{X}_3 \\
\boldsymbol{F}_3 = -b_3 \boldsymbol{F}_1 - 3b_4 X_3^2 \boldsymbol{V}_3.
\end{cases}
\tag{A4}
$$

A2 Gold Coast

Considering only the terms with a variance of $Var_{eq} \geq 10\%$ (see Table 3) leads to:

$$
\begin{cases}
\dot{X}_1 = X_2 \\
\dot{X}_2 = -a_9 X_1^3 + a_5 X_1 - a_1 X_3 \\
\dot{X}_3 = b_3 X_2 - b_5 X_1^2.
\end{cases}
\tag{A5}
$$

Defining the second order derivatives, we get:

$$
\begin{cases}
\ddot{X}_1 = -a_9 X_1^3 + a_5 X_1 - a_1 X_3 \\
\ddot{X}_3 = b_3 \ddot{X}_1 - 2b_5 \dot{X}_1 X_1,
\end{cases}
\tag{A6}
$$

705   and then:

$$
\begin{cases}
\boldsymbol{A}_1 = -a_9 X_1^2 \boldsymbol{X_1} + a_5 \boldsymbol{X_1} - a_1 \boldsymbol{X_3} \\
\boldsymbol{A}_3 = b_3 \boldsymbol{A}_1 - 2b_5 X_1 \boldsymbol{V}_1,
\end{cases}
\tag{A7}
$$

with $\boldsymbol{A_i}$ and $\boldsymbol{V_i}$ the sand mass acceleration and speed, respectively. Under the hypothesis that both masses are equal ($m_1 = m_3$), we can view the problem as the force applied to the sand masses as:

$$
\begin{cases}
\boldsymbol{F}_1 = -a_9 X_1^2 \boldsymbol{X_1} + a_5 \boldsymbol{X_1} - a_1 \boldsymbol{X_3}, \\
\boldsymbol{F}_3 = b_3 \boldsymbol{F}_1 - 2b_5 X_1 \boldsymbol{V}_1.
\end{cases}
\tag{A8}
$$

710   **A3   Ensenada**

Considering only the terms with a variance of $Var_{eq} \geq 10\%$ (see Table 4) leads to:

$$
\begin{cases}
\dot{X}_1 = X_2 \\
\dot{X}_2 = -a_8 X_1^3 - a_6 X_1^2 X_3 + a_1 X_3 \\
\dot{X}_3 = -b_3 X_2 + b_4 X_2^3.
\end{cases}
\tag{A9}
$$

Defining the second order derivatives, we get:

$$
\begin{cases}
\ddot{X}_1 = -a_8 X_1^3 - a_6 X_1^2 X_3 + a_1 X_3 \\
\ddot{X}_3 = -b_3 \ddot{X}_1 + 3b_4 X_2^2 \dot{X}_2,
\end{cases}
\tag{A10}
$$

715   and then:

$$
\begin{cases}
\boldsymbol{A}_1 = -a_8 X_1^2 \boldsymbol{X_1} - a_6 X_1^2 \boldsymbol{X_3} + a_1 \boldsymbol{X_3} \\
\boldsymbol{A}_3 = -b_3 \boldsymbol{A}_1 + 3b_4 X_2^2 \boldsymbol{A}_1,
\end{cases}
\tag{A11}
$$

with $\boldsymbol{A_i}$ and $\boldsymbol{V_i}$ the sand mass acceleration and speed, respectively. Under the hypothesis that both masses are equal ($m_1 = m_3$), we can view the problem as the force applied to the sand masses as:

$$\begin{cases} \boldsymbol{F}_1 = -a_8 X_1^2 \boldsymbol{X_1} - a_6 X_1^2 \boldsymbol{X_3} + a_1 \boldsymbol{X_3}, \\ \boldsymbol{F}_3 = -b_3 \boldsymbol{F}_1 + 3b_4 X_2^2 \boldsymbol{F}_1. \end{cases} \tag{A12}$$

720 **A4   Duck**

Considering only the terms with a variance of $Var_{eq} \geq 10\%$ (see Table 5) leads to:

$$\begin{cases} \dot{X}_1 = X_2 \\ \dot{X}_2 = a_4 X_2^2 X_3 - a_5 X_2^3 - a_{11} X_1 X_2 X_4 - a_{11} X_1 X_2^2 - a_8 X_1 X_4^2 \\ \dot{X}_3 = X_4 \\ \dot{X}_4 = -c_1 X_3^3 + c_3 X_1. \end{cases} \tag{A13}$$

Defining the second order derivatives, we get:

$$\begin{cases} \ddot{X}_1 = a_4 X_2^2 X_3 - a_5 X_2^3 - a_{11} X_1 X_2 X_4 - a_{11} X_1 X_2^2 - a_8 X_1 X_4^2 \\ \ddot{X}_3 = -c_1 X_3^3 + c_3 X_1, \end{cases} \tag{A14}$$

725 and then:

$$\begin{cases} \boldsymbol{A}_1 = a_4 X_2^2 \boldsymbol{X_3} - a_5 X_2^2 \boldsymbol{X_2} - a_{11} X_1 X_2 \boldsymbol{X_4} - a_{11} \boldsymbol{X_1} X_2^2 - a_8 \boldsymbol{X_1} X_4^2 \\ \boldsymbol{A}_3 = -c_1 X_3^2 \boldsymbol{X_3} + c_3 \boldsymbol{X_1}, \end{cases} \tag{A15}$$

with $\boldsymbol{A_i}$ and $\boldsymbol{V_i}$ the sand mass acceleration and speed, respectively. Under the hypothesis that both masses are equal ($m_1 = m_3$), we can view the problem as the force applied to the sand masses as:

$$\begin{cases} \boldsymbol{F}_1 = a_4 X_2^2 \boldsymbol{X_3} - a_5 X_2^2 \boldsymbol{X_2} - a_{10} X_1 X_2 \boldsymbol{X_4} - a_{11} X_2^2 \boldsymbol{X_1} - a_8 X_4^2 \boldsymbol{X_1}, \\ \boldsymbol{F}_3 = c_1 X_3^2 \boldsymbol{X_3} + c_3 X_1^2 \boldsymbol{X_1}. \end{cases} \tag{A16}$$

730 *Code availability.* The GPoM R-package used in this study can be found at: 10.32614/CRAN.package.GPoM

Data availability. The raw satellite-derived shoreline and sandbar positions used in this study can be found at: 10.5281/zenodo.18220531

Author contributions. S.F., S.M., and M.A. wrote and proofread the manuscript. All authors contributed to the scientific work and discussion. All authors reviewed the manuscript.

Competing interests. The authors declare no competing interest.

735 *Financial support.* This study has been partially supported through the grant EUR TESS N°ANR-18-EURE-0018 in the framework of the Programme des Investissements d'Avenir.

References

Aguirre, L. A. and Letellier, C.: Modeling Nonlinear Dynamics and Chaos: A Review, Mathematical Problems in Engineering, 2009, 238 960, https://doi.org/https://doi.org/10.1155/2009/238960, 2009.

740   Aguirre, L. A., Portes, L. L., and Letellier, C.: Structural, dynamical and symbolic observability: From dynamical systems to networks, PLoS One, 13, e0206 180, 2018.

Ahnert, K. and Abel, M.: Numerical differentiation of experimental data: local versus global methods, Computer Physics Communications, 177, 764–774, 2007.

Almar, R., Boucharel, J., Graffin, M., Abessolo, G. O., Thoumyre, G., Papa, F., Ranasinghe, R., Montano, J., Bergsma, E. W. J.,

745   Baba, M. W., and Jin, F.-F.: Influence of El Niño on the variability of global shoreline position, Nature Communications, 14, 3133, https://doi.org/10.1038/s41467-023-38742-9, 2023.

Anderson, D., Bak, A. S., Cohn, N., Brodie, K. L., Johnson, B., and Dickhudt, P.: The Impact of Inherited Morphology on Sandbar Migration During Mild Wave Seasons, Geophysical Research Letters, 50, e2022GL101 219, https://doi.org/10.1029/2022GL101219, 2023.

Aubrey, D. G., Inman, D. L., and Winant, C. D.: The statistical prediction of beach changes in southern California, Journal of Geophysical

750   Research, 85, 3264, https://doi.org/10.1029/JC085iC06p03264, 1980.

Baas, A. C.: Chaos, fractals and self-organization in coastal geomorphology: simulating dune landscapes in vegetated environments, Geomorphology, 48, 309–328, https://doi.org/10.1016/S0169-555X(02)00187-3, 2002.

Benettin, G., Galgani, L., Giorgilli, A., and Strelcyn, J.-M.: Lyapunov characteristic exponents for smooth dynamical systems and for Hamiltonian systems; a method for computing all of them. Part 1: Theory, Meccanica, 15, 9–20, 1980.

755   Bergé, P., Pomeau, Y., and Vidal, C.: Order within chaos, 1986.

Bergsma, E. W. J., Klotz, A. N., Artigues, S., Graffin, M., Prenowitz, A., Delvit, J.-M., and Almar, R.: Shoreliner: A Sub-Pixel Coastal Waterline Extraction Pipeline for Multi-Spectral Satellite Optical Imagery, Remote Sensing, 16, 2795, https://doi.org/10.3390/rs16152795, number: 15 Publisher: Multidisciplinary Digital Publishing Institute, 2024.

Brunton, S. L., Proctor, J. L., and Kutz, J. N.: Discovering governing equations from data by sparse identification of nonlinear dynamical

760   systems, Proceedings of the national academy of sciences, 113, 3932–3937, 2016.

Castelle, B. and Masselink, G.: Morphodynamics of wave-dominated beaches, Cambridge Prisms: Coastal Futures, 1, e1, https://doi.org/10.1017/cft.2022.2, 2023.

Castelle, B., Kras, E., Masselink, G., Scott, T., Konstantinou, A., and Luijendijk, A.: Satellite-derived sandy shoreline trends and interannual variability along the Atlantic coast of Europe, preprint, In Review, https://doi.org/10.21203/rs.3.rs-3696677/v1, 2023.

765   Chander, G., Markham, B. L., and Helder, D. L.: Summary of current radiometric calibration coefficients for Landsat MSS, TM, ETM+, and EO-1 ALI sensors, Remote Sensing of Environment, 113, 893–903, https://doi.org/10.1016/j.rse.2009.01.007, 2009.

Charó, G. D., Chekroun, M. D., Sciamarella, D., and Ghil, M.: Noise-driven topological changes in chaotic dynamics, Chaos: An Interdisciplinary Journal of Nonlinear Science, 31, 2021.

Cipolletti, M. P., Delrieux, C. A., Perillo, G. M. E., and Cintia Piccolo, M.: Superresolution border segmentation and measurement in remote

770   sensing images, Computers & Geosciences, 40, 87–96, https://doi.org/10.1016/j.cageo.2011.07.015, 2012.

Coco, G. and Murray, A. B.: Patterns in the sand: From forcing templates to self-organization, Geomorphology, 91, 271–290, https://doi.org/10.1016/j.geomorph.2007.04.023, 2007.

Davidson, M., Splinter, K., and Turner, I.: A simple equilibrium model for predicting shoreline change, Coastal Engineering, 73, 191–202, https://doi.org/10.1016/j.coastaleng.2012.11.002, 2013.

775 Dean, R. G.: Equilibrium beach profiles: characteristics and applications, Journal of coastal research, pp. 53–84, 1991.

Di Capua, G., Coumou, D., van den Hurk, B., Weisheimer, A., Turner, A. G., and Donner, R. V.: Validation of boreal summer tropical–extratropical causal links in seasonal forecasts, Weather and Climate Dynamics, 4, 701–723, https://doi.org/10.5194/wcd-4-701-2023, 2023.

Dijkstra, H. A.: Nonlinear climate dynamics, Cambridge University Press, 2013.

780 Ding, M., Grebogi, C., Ott, E., Sauer, T., and Yorke, J. A.: Plateau onset for correlation dimension: When does it occur?, Physical Review Letters, 70, 3872, 1993.

Eckmann, J.-P. and Ruelle, D.: Fundamental limitations for estimating dimensions and Lyapunov exponents in dynamical systems, Physica D: Nonlinear Phenomena, 56, 185–187, 1992.

Frugier, S., Almar, R., Bergsma, E., and Granjou, A.: SBI: A sandbar extraction spectral index for multi-spectral satellite optical imagery,
785 Coastal Engineering, 200, 104 752, https://doi.org/https://doi.org/10.1016/j.coastaleng.2025.104752, 2025.

Frugier, S., Almar, R., Bergsma, E. W., and Bak, S. A.: Standalone color-based bathymetry over 10 years at Duck (NC, USA) from optical satellite imagery and wave breaking analysis, Coastal Engineering, 203, 104 855, https://doi.org/https://doi.org/10.1016/j.coastaleng.2025.104855, 2026.

Gander, W.: Algorithms for the QR decomposition, Res. Rep, 80, 1251–1268, 1980.

790 Ghil, M. and Sciamarella, D.: Review article: Dynamical systems, algebraic topology and the climate sciences, Nonlinear Processes in Geophysics, 30, 399–434, https://doi.org/10.5194/npg-30-399-2023, 2023.

Gilmore, R. and Lefranc, M.: The topology of chaos: Alice in stretch and squeezeland, John Wiley & Sons, 2002.

Gorelick, N., Hancher, M., Dixon, M., Ilyushchenko, S., Thau, D., and Moore, R.: Google Earth Engine: Planetary-scale geospatial analysis for everyone, Remote Sensing of Environment, 202, 18–27, https://doi.org/10.1016/j.rse.2017.06.031, 2017.

795 Gouesbet, G. and Letellier, C.: Global vector-field reconstruction by using a multivariate polynomial L 2 approximation on nets, Physical Review E, 49, 4955, 1994.

Graffin, M., Almar, R., Bergsma, E. W. J., Boucharel, J., Vitousek, S., Taherkhani, M., and Ruggiero, P.: Waterline responses to climate forcing along the North American West Coast, Communications Earth & Environment, 6, 444, https://doi.org/10.1038/s43247-025-02414-x, 2025a.

800 Graffin, M., Touzé, T., Bergsma, E. W., and Almar, R.: Towards a global assessment of sandy shorelines: Systematic extraction and validation of optical satellite-derived coastal indicators at various sites, Remote Sensing of Environment, 331, 115 033, https://doi.org/https://doi.org/10.1016/j.rse.2025.115033, 2025b.

Grassberger, P. and Procaccia, I.: Characterization of Strange Attractors, Physical Review Letters, 50, 346–349, https://doi.org/10.1103/PhysRevLett.50.346, 1983.

805 Grond, F., Diebner, H. H., Sahle, S., Mathias, A., Fischer, S., and Rossler, O. E.: A robust, locally interpretable algorithm for Lyapunov exponents, Chaos, Solitons & Fractals, 16, 841–852, 2003.

Guo, Z., Lyu, P., Ling, F., Bai, L., Luo, J.-J., Boers, N., Yamagata, T., Izumo, T., Cravatte, S., Capotondi, A., and Ouyang, W.: Data-driven global ocean modeling for seasonal to decadal prediction, Science Advances, 11, eadu2488, https://doi.org/10.1126/sciadv.adu2488, 2025.

Jardak, M. and Talagrand, O.: Ensemble variational assimilation as a probabilistic estimator – Part 2: The fully non-linear case, Nonlinear
810 Processes in Geophysics, 25, 589–604, https://doi.org/10.5194/npg-25-589-2018, 2018.

Jerolmack, D. J. and Paola, C.: Shredding of environmental signals by sediment transport: SIGNAL SHREDDING, Geophysical Research Letters, 37, n/a–n/a, https://doi.org/10.1029/2010GL044638, 2010.

Jin, F.-F., Neelin, J. D., and Ghil, M.: El Niño on the devil's staircase: Annual subharmonic steps to chaos, Science, 264, 70–72, 1994.

Kaplan, J. and Yorke, J.: Chaotic behavior of multidimensional difference equations, pp. 204–227, 730, Springer, 1979.

815   Konstantinou, A., Scott, T., Masselink, G., Stokes, K., Conley, D., and Castelle, B.: Satellite-based shoreline detection along high-energy macrotidal coasts and influence of beach state, Marine Geology, 462, 107 082, https://doi.org/10.1016/j.margeo.2023.107082, 2023.

Langford, W. F.: Numerical Studies of Torus Bifurcations, pp. 285–295, Birkhäuser Basel, Basel, ISBN 978-3-0348-6256-1, https://doi.org/10.1007/978-3-0348-6256-1_19, 1984.

Letellier, C. and Aguirre, L. A.: Required criteria for recognizing new types of chaos: Application to the "cord" attractor, Phys. Rev. E, 85,
820   036 204, https://doi.org/10.1103/PhysRevE.85.036204, 2012.

Letellier, C. and Gilmore, R.: Introduction to topological analysis, in: Topology and Dynamics of Chaos: In Celebration of Robert Gilmore's 70th Birthday, pp. 1–19, World Scientific, 2013.

Letellier, C., Le Sceller, L., Maréchal, E., Dutertre, P., Maheu, B., Gouesbet, G., Fei, Z., and Hudson, J.: Global vector field reconstruction from a chaotic experimental signal in copper electrodissolution, Physical review E, 51, 4262, 1995.

825   Letellier, C., Aguirre, L. A., and Freitas, U. S.: Frequently asked questions about global modeling, Chaos: An Interdisciplinary Journal of Nonlinear Science, 19, 023 103, https://doi.org/10.1063/1.3125705, 2009.

Letellier, C., Sendiña-Nadal, I., Bianco-Martinez, E., and Baptista, M. S.: A symbolic network-based nonlinear theory for dynamical systems observability, Scientific reports, 8, 3785, 2018.

Letellier, C., Olsen, L. F., and Mangiarotti, S.: Chaos: From theory to applications for the 80th birthday of Otto E. Rössler, Chaos: An
830   Interdisciplinary Journal of Nonlinear Science, 31, 2021.

Lippmann, T. C. and Holman, R. A.: Quantification of sand bar morphology: A video technique based on wave dissipation, Journal of Geophysical Research: Oceans, 94, 995–1011, https://doi.org/10.1029/JC094iC01p00995, _eprint: https://onlinelibrary.wiley.com/doi/pdf/10.1029/JC094iC01p00995, 1989.

Lippmann, T. C. and Holman, R. A.: The spatial and temporal variability of sand bar morphology, Journal of Geophysical Research: Oceans,
835   95, 11 575–11 590, https://doi.org/https://doi.org/10.1029/JC095iC07p11575, 1990.

Lorenz, E. N.: Deterministic Nonperiodic Flow, Journal of Atmospheric Sciences, 20, 130 – 141, https://doi.org/10.1175/1520-0469(1963)020<0130:DNF>2.0.CO;2, 1963.

Lorenz, E. N.: The local structure of a chaotic attractor in four dimensions, Physica D: nonlinear phenomena, 13, 90–104, 1984.

Lovejoy, S.: Weather, macroweather, and the climate: our random yet predictable atmosphere, Oxford University Press, 2019.

840   Ludka, B. C., Guza, R. T., O'Reilly, W. C., Merrifield, M. A., Flick, R. E., Bak, A. S., Hesser, T., Bucciarelli, R., Olfe, C., Woodward, B., Boyd, W., Smith, K., Okihiro, M., Grenzeback, R., Parry, L., and Boyd, G.: Sixteen years of bathymetry and waves at San Diego beaches, Scientific Data, 6, 161, https://doi.org/10.1038/s41597-019-0167-6, 2019.

Luijendijk, A., Hagenaars, G., Ranasinghe, R., Baart, F., Donchyts, G., and Aarninkhof, S.: The State of the World's Beaches, Scientific Reports, 8, 6641, https://doi.org/10.1038/s41598-018-24630-6, 2018.

845   Mangiarotti, S.: Low dimensional chaotic models for the plague epidemic in Bombay (1896–1911), Chaos, Solitons & Fractals, 81, 184–196, https://doi.org/10.1016/j.chaos.2015.09.014, 2015.

Mangiarotti, S. and Huc, M.: Can the original equations of a dynamical system be retrieved from observational time series?, Chaos: An Interdisciplinary Journal of Nonlinear Science, 29, 023 133, https://doi.org/10.1063/1.5081448, 2019.

Mangiarotti, S. and Le Jean, F.: Chaotic attractors captured from remote sensing time series for the dynamics of cereal crops, Journal of
850   Difference Equations and Applications, 29, 1480–1502, https://doi.org/10.1080/10236198.2022.2152336, 2023.

Mangiarotti, S., Coudret, R., Drapeau, L., and Jarlan, L.: Polynomial search and global modeling: Two algorithms for modeling chaos,
Physical Review E, 86, 046 205, https://doi.org/10.1103/PhysRevE.86.046205, 2012.

Mangiarotti, S., Peyre, M., and Huc, M.: A chaotic model for the epidemic of Ebola virus disease in West Africa (2013–2016), Chaos: An
Interdisciplinary Journal of Nonlinear Science, 26, 113 112, https://doi.org/10.1063/1.4967730, 2016.

855   Mangiarotti, S., Saéz, M., Benavente, D., Pla, C., Tran, M., Bottinelli, N., and Jouquet, P.: Governing equations and topology extracted from
observational time series in environmental sciences, in: From nonlinear dynamical systems to observational chaos, edited by Letellier, C.
and Mangiarotti, S., pp. 142–148, Toulouse, France, 2023.

Mangiarotti, S., Neuhauser, M., Arnaud, L., Bach Nguyen, T., and Verrier, S.: Inference of couplings between variables of a given system us-
ing causal wavelets, causal information, equations reconstruction, and other techniques, Chaos: An Interdisciplinary Journal of Nonlinear
860   Science, 35, 103 124, https://doi.org/10.1063/5.0272112, 2025.

Mangiarotti, S. et al.: Modélisation globale et caractérisation topologique de dynamiques environnementales: de l'analyse des enveloppes
fluides et du couvert de surface de la Terre à la caractérisation topolodynamique du chaos, Habilitation to direct Researches, Université de
Toulouse, 3, 2014.

Mao, Y., Coco, G., Vitousek, S., Antolinez, J. A., Azorakos, G., Banno, M., Bouvier, C., Bryan, K. R., Cagigal, L., Calcraft, K., et al.:
865   Benchmarking shoreline prediction models over multi-decadal timescales, Communications Earth & Environment, 6, 581, 2025.

Maraldi, B., Dijkstra, H. A., and Ghil, M.: Intraseasonal atmospheric variability under climate trends, Chaos: An Interdisciplinary Journal of
Nonlinear Science, 35, 053 136, https://doi.org/10.1063/5.0253103, 2025.

Masselink, G. and Short, A. D.: The Effect of Tide Range on Beach Morphodynamics and Morphology: A Conceptual Beach Model,
Journalof CoastalResearch, 9, 1993.

870   May, R. M.: Simple mathematical models with very complicated dynamics, Nature, 261, 459–467, 1976.

Mindlin, G. and Gilmore, R.: Topological Analysis of Chaotic Time Series, in: Proceedings Of The 1st Experimental Chaos Conference,
p. 31, World Scientific, 1992.

Murray, A. B., Lazarus, E., Ashton, A., Baas, A., Coco, G., Coulthard, T., Fonstad, M., Haff, P., McNamara, D., Paola, C., Pelletier,
J., and Reinhardt, L.: Geomorphology, complexity, and the emerging science of the Earth's surface, Geomorphology, 103, 496–505,
875   https://doi.org/10.1016/j.geomorph.2008.08.013, 2009.

Murray, A. B., Coco, G., and Goldstein, E. B.: Cause and effect in geomorphic systems: Complex systems perspectives, Geomorphology,
214, 1–9, https://doi.org/10.1016/j.geomorph.2014.03.001, 2014.

Nicolis, G. and Nicolis, C.: Nonlinear dynamic systems in the geosciences, Bulletin (Kansas Geological Survey), pp. 33–42, 1991.

Otsu, N.: A Threshold Selection Method from Gray-Level Histograms, IEEE Transactions on Systems, Man, and Cybernetics, 9, 62–66,
880   https://doi.org/10.1109/TSMC.1979.4310076, conference Name: IEEE Transactions on Systems, Man, and Cybernetics, 1979.

Ott, E.: Strange attractors and fractal dimension, p. 71–114, Cambridge University Press, 2002.

Pianca, C., Holman, R., and Siegle, E.: Shoreline variability from days to decades: Results of long-term video imaging, Journal of Geophys-
ical Research: Oceans, 120, 2159–2178, https://doi.org/10.1002/2014JC010329, 2015.

Plant, N. G., Holman, R. A., Freilich, M. H., and Birkemeier, W. A.: A simple model for interannual sandbar behavior, Journal of Geophysical
885   Research: Oceans, 104, 15 755–15 776, https://doi.org/https://doi.org/10.1029/1999JC900112, 1999.

Poincaré, H.: Les méthodes nouvelles de la mécanique céleste, vol. 2, Gauthier-Villars et fils, imprimeurs-libraires, 1893.

Price, T., Rutten, J., and Ruessink, B.: Coupled behaviour within a double sandbar system, Journal of Coastal Research, pp. 125–129, http://www.jstor.org/stable/26482146, 2011.

QGIS Development Team: QGIS Geographic Information System, Open Source Geospatial Foundation, http://qgis.org, 2025.

890   Reeve, D. E., Pedrozo-Acuña, A., and Spivack, M.: Beach memory and ensemble prediction of shoreline evolution near a groyne, Coastal Engineering, 86, 77–87, https://doi.org/https://doi.org/10.1016/j.coastaleng.2013.11.010, 2014.

Rosalie, M. and Letellier, C.: Toward a General Procedure for Extracting Templates from Chaotic Attractors Bounded by High Genus Torus, International Journal of Bifurcation and Chaos, 24, 1450 045, https://doi.org/10.1142/S021812741450045X, 2014.

Rosalie, M. and Mangiarotti, S.: Structure analysis of the Lorenz-84 chaotic attractor, Chaos: An Interdisciplinary Journal of Nonlinear
895   Science, 35, 103 101, https://doi.org/10.1063/5.0287725, 2025.

Rössler, O. E.: An equation for hyperchaos, Physics Letters A, 71, 155–157, 1979.

Rössler, O. E.: The chaotic hierarchy, Zeitschrift für Naturforschung A, 38, 788–801, 1983.

Ruelle, D.: A measure associated with axiom-A attractors, American Journal of Mathematics, pp. 619–654, 1976.

Ruessink, B., Pape, L., and Turner, I.: Daily to interannual cross-shore sandbar migration: Observations from a multiple sandbar system,
900   Continental Shelf Research, 29, 1663–1677, https://doi.org/https://doi.org/10.1016/j.csr.2009.05.011, 2009.

Ruessink, B. G., Wijnberg, K. M., Holman, R. A., Kuriyama, Y., and van Enckevort, I. M. J.: Intersite comparison of interannual nearshore bar behavior, Journal of Geophysical Research: Oceans, 108, https://doi.org/https://doi.org/10.1029/2002JC001505, 2003.

Ruessink, B. G., Coco, G., Ranasinghe, R., and Turner, I. L.: Coupled and noncoupled behavior of three-dimensional morphological patterns in a double sandbar system, Journal of Geophysical Research: Oceans, 112, 2006JC003 799, https://doi.org/10.1029/2006JC003799, 2007.

905   Ruiz, J., Ailliot, P., Chau, T. T. T., Le Bras, P., Monbet, V., Sévellec, F., and Tandeo, P.: Analog data assimilation for the selection of suitable general circulation models, Geoscientific Model Development, 15, 7203–7220, https://doi.org/10.5194/gmd-15-7203-2022, 2022.

Ruiz De Alegría-Arzaburu, A. and Vidal-Ruiz, J. A.: Beach recovery capabilities after El Niño 2015–2016 at Ensenada Beach, Northern Baja California, Ocean Dynamics, 68, 749–759, https://doi.org/10.1007/s10236-018-1164-6, 2018.

Sauer, T., Yorke, J. A., and Casdagli, M.: Embedology, Journal of statistical Physics, 65, 579–616, 1991.

910   Sciamarella, D. and Charó, G. D.: New elements for a theory of chaos topology, in: Topological Methods for Delay and Ordinary Differential Equations: With Applications to Continuum Mechanics, pp. 191–211, Springer, 2024.

Simmons, J. A. and Splinter, K. D.: Data-driven shoreline modelling at timescales of days to years, Coastal Engineering, 197, 104 685, 2025.

Takens, F.: Detecting strange attractors in turbulence, in: Dynamical Systems and Turbulence, Warwick 1980, edited by Rand, D. and Young, L.-S., pp. 366–381, Springer Berlin Heidelberg, Berlin, Heidelberg, ISBN 978-3-540-38945-3, 1981.

915   Vos, K., Harley, M. D., Splinter, K. D., Walker, A., and Turner, I. L.: Beach Slopes From Satellite-Derived Shorelines, Geophysical Research Letters, 47, e2020GL088 365, https://doi.org/10.1029/2020GL088365, 2020.

Vos, K., Splinter, K. D., Palomar-Vázquez, J., Pardo-Pascual, J. E., Almonacid-Caballer, J., Cabezas-Rabadán, C., Kras, E. C., Luijendijk, A. P., Calkoen, F., Almeida, L. P., Pais, D., Klein, A. H. F., Mao, Y., Harris, D., Castelle, B., Buscombe, D., and Vitousek, S.: Benchmarking satellite-derived shoreline mapping algorithms, Communications Earth & Environment, 4, 345, https://doi.org/10.1038/s43247-023-
920   01001-2, 2023.

Whaley III, D. L.: The interquartile range: Theory and estimation, Master's thesis, East Tennessee State University, 2005.

Winant, C. D., Inman, D. L., and Nordstrom, C. E.: Description of seasonal beach changes using empirical eigenfunctions, Journal of Geophysical Research (1896-1977), 80, 1979–1986, https://doi.org/https://doi.org/10.1029/JC080i015p01979, 1975.

Wolf, A., Swift, J. B., Swinney, H. L., and Vastano, J. A.: Determining Lyapunov exponents from a time series, Physica D: nonlinear

925   phenomena, 16, 285–317, 1985.

Wright, L. D. and Short, A. D.: MORPHODYNAMIC VARIABILITY OF SURF ZONES AND BEACHES: A SYNTHE:~IS, 1984.

Yates, M. L., Guza, R. T., and O'Reilly, W. C.: Equilibrium shoreline response: Observations and modeling, Journal of Geophysical Research,
114, C09 014, https://doi.org/10.1029/2009JC005359, 2009.